A Maximum-Likelihood-Based Two-User Receiver for LoRa Chirp Spread-Spectrum Modulation

Mathieu Xhonneux, *Graduate Student Member, IEEE*, Joachim Tapparel, Alexios Balatsoukas-Stimming, *Member, IEEE*, Andreas Burg, *Senior Member, IEEE*, and Orion Afisiadis, *Member, IEEE*

***Abstract*—Long Range (LoRa) is an emerging low-power wide-area network technology offering long-range wireless connectivity to Internet of Things (IoT) devices. For energy efficiency reasons, LoRa end nodes implement a nonslotted ALOHA multiple access scheme to transmit packets to the gateway. Due to the lack of synchronization between end nodes, collisions between uplink packets have been identified as the main obstacle to the scaling of dense LoRa networks. To tackle this issue, we present in this article a LoRa receiver that is capable of decoding colliding packets from two interfering end nodes. The proposed two-user detector is derived from the maximum-likelihood principle using a detailed model of two colliding LoRa packets. As the complexity of the maximum-likelihood sequence estimation is prohibitive, complexity-reduction techniques are introduced to enable practical implementations of the receiver. An in-depth performance analysis highlights that the proposed two-user detector inherently leverages the differences in received power, time offsets, and frequency offsets between the users to separate and demodulate their respective signals. To demonstrate the practicality of the proposed detector, an interference-robust synchronization algorithm is then designed and evaluated. Simulation results indicate that a LoRa receiver combining the proposed synchronization algorithm and two-user detector is capable of detecting and demodulating two interfering users with satisfactorily error rates.**

***Index Terms*—Internet of Things (IoT) standards, long range (LoRa), low-power wide-area networks (LPWANs), multiuser receivers, synchronization.**

I. Introduction

In THE last years, the emergence of energy-constrained Internet of Things (IoT) devices called for the development of new low-power wide-area network (LPWAN) standards [1]. LPWANs aim to connect IoT devices to gateways over large distances while minimizing the energy overhead of the transmissions for the end nodes. Unlike the energy-intensive 3GPP cellular standards, such as NB-IoT and LTE-M, LPWAN standards rely on low-complexity physical (PHY) and medium access control (MAC) layers. Among the new LPWAN technologies, LoRa has become one of the most popular and widely deployed protocols [2], [3]. The LoRa physical layer is proprietary, but its chirp spread-spectrum modulation has recently been studied extensively in [4]–[9], even for localization [10]. The MAC layer, named LoRaWAN, is an open standard defined by the LoRa Alliance [11].

At the PHY layer, LoRa uses a chirp spread-spectrum modulation allowing receivers to demodulate signals with received powers even below the noise floor [12]. The spreading gain of the LoRa modulation is determined by the spreading factor (SF), which allows to tradeoff transmission time and data rate for coverage. The highest SFs enable end nodes to communicate with a gateway over distances up to 15–30 km [13], [14]. At the MAC layer, to avoid an energy-intensive synchronization mechanism between users, LoRaWAN implements a nonslotted ALOHA multiple access scheme [15]. As the end nodes are not synchronized and share nonorthogonal waveforms, collisions between users may arise and frequently pose a threat to the scalability of future massive LoRa IoT systems [16].

In particular, scalability studies have shown that the throughput of a LoRa network decreases rapidly for an increasing number of users, as a result of the collisions [17]–[19]. To prevent the end nodes from colliding, several papers suggested to transform LoRaWAN into a slotted ALOHA scheme [20], or to deploy scheduling algorithms at the gateway for distributing time slots among the users [21]–[24]. Such solutions however complexify the MAC layer and imply significant energy overhead for the end nodes. In this work, we seek instead to improve the scalability of LoRaWAN networks by resorting to multiuser receivers at the gateways, which have almost no power constraints. Multiuser receivers allow to increase the throughput of ALOHA networks without requiring any modifications to the MAC layer by decoding concurrent transmissions [25]. Fig. 1 shows that in a nonslotted ALOHA network, a two-user receiver may theoretically reach a maximum throughput that is three times higher than a conventional single-user receiver, thanks to its ability to recover two colliding packets.

Considering more specifically LoRa communications, we first notice that interference between colliding LoRa users can be one of two very different types: 1) *inter-SF interference* and 2) *same-SF interference*. Due to the spreading, the impact of inter-SF interference is different than the impact of same-SF

Manuscript received 13 April 2022; accepted 16 June 2022. Date of publication 28 June 2022; date of current version 7 November 2022. *(Corresponding author: Mathieu Xhonneux.)*

Mathieu Xhonneux is with ICTEAM, Université catholique de Louvain, 1348 Louvain-la-Neuve, Belgium (e-mail: mathieu.xhonneux@uclouvain.be).

Joachim Tapparel, Andreas Burg, and Orion Afisiadis are with the Telecommunications Circuits Laboratory, École Polytechnique Fédérale de Lausanne, 1015 Lausanne, Switzerland.

Alexios Balatsoukas-Stimming is with the Department of Electrical Engineering, Eindhoven University of Technology, 5612 AZ Eindhoven, The Netherlands.

Digital Object Identifier 10.1109/JIOT.2022.3186732

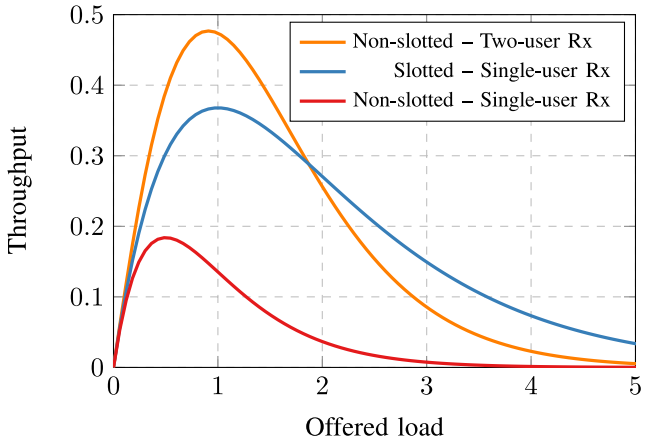

Fig. 1. Theoretical throughputs of nonslotted ALOHA and slotted ALOHA networks. Two-user receivers strongly improve the throughput of nonslotted ALOHA networks as they are capable of decoding two colliding packets.

interference. Notably, LoRa transmissions using different SFs only suffer from inter-SF interference at very low signal-to-interference ratios (SIR) (starting from around −16 dB on average) thanks to near-orthogonal signaling [26]. Since concurrent transmissions on different SFs can be demodulated independently in parallel, commercial LoRa gateways embed several demodulators that can be dynamically assigned to different SFs. On the other hand, simultaneous transmissions with the same SF are far from orthogonal [27], [28]. For existing single-user LoRa receivers, colliding packets with the same SF exhibit a capture effect, such that the strongest signal can often be demodulated if the SIR and the signal-to-noise ratio (SNR) are sufficient, but at the expense of the weaker signal [28]. Experimental measurements have shown that for a 3-dB difference in power between two users, there is a 97% chance of demodulating the packet of the strongest user [29], but the packet of the weaker user is generally lost.

Several LoRa multiuser receivers have recently been suggested [30]–[35]. In [30], a successive interference cancelation (SIC) receiver that relies on the conventional single-user detector is proposed. A multiuser receiver based on nonstationary signal scaling to separate superimposed transmissions is presented in [31], whereas Tong *et al.* [34] leveraged the time offsets between colliding packets to separate and demodulate their symbols. Hu *et al.* [32] and Xia *et al.* [33] suggested to first demodulate all symbols and then to assign them to their respective transmitters based on the differences of time and power between users. Similarly, a parallel interference cancelation receiver that relies on the differences in carrier frequencies and received powers between users is derived in [35]. The aforementioned works designed multiuser receivers that heuristically leverage one or two transmitter-specific features (e.g., carrier offset, time offset, and received powers) to distinguish the contributions of the respective users. These receivers however fail to attain useful error rates at the low SNRs that are characteristic for LoRa communications. A practical multiuser receiver derived from the maximum likelihood (ML) principle that optimally uses all properties of a signal with two colliding LoRa users to operate even at low SNR is hence still missing in the literature.

Contributions: In this work, we provide a detailed description of the two-user LoRa receiver initially introduced in [36]. This two-user receiver features a detector that is derived from the ML sequence estimator (MLSE) and performs individual decisions on the interfering symbols instead of a joint detection over the entire colliding frames. Whereas Xhonneux *et al.* [36] only provided limited experimental results from a proof-of-concept testbed, we conduct in this article a full derivation and performance analysis of the proposed receiver. We show that the described detector inherently leverages the difference of time, carrier frequency, and received power between users to demodulate the colliding symbols. We highlight that the carrier frequency offset (CFO) and the sampling time offset (STO) of a user modify the spectral representation of its symbols. Simulation results notably show that desynchronized users are easier to jointly demodulate than the closely synchronized users, as their symbols are less correlated. Since the derived detector requires estimates of the CFO, the STO, and the power of each colliding user, we also present in this article an improved version of the multiuser synchronization algorithm from [36]. The overall two-user LoRa receiver, which combines interference-resilient synchronization and two-user detection, shows satisfactorily performance with low error rates even at low SNRs.

Outline: The remainder of this article is organized as follows. In Section II, we provide a summary of the LoRa modulation, single-user demodulation process, and preamble of a LoRa packet. We then describe in detail the signal model of two interfering LoRa users sharing the same SF. In Section III, we derive a practical two-user detector from the MLSE using different complexity reduction techniques. In Section IV, we evaluate the performance of the proposed detector with simulation results. Different parameters influencing the error rates of the receiver are discussed. In Section V, we present a multiuser synchronization algorithm that is robust to same-SF interference, and we jointly evaluate its performance together with the proposed two-user detector.

II. Principles of the LoRa PHY

In this section, we provide a brief summary of the LoRa modulation, the single-user demodulation stage, and the structure of the preamble. We then explain the baseband-equivalent model of two superimposed LoRa signals.

A. Modulation and Demodulation

LoRa is a chirp spread-spectrum modulation operating in the industrial, scientific, and medical (ISM) bands, with typical passband bandwidth values of $B \in \{125, 250, 500\}$ kHz. LoRa symbols are chirps, i.e., signals whose instantaneous frequency increases linearly and spans the entire bandwidth. Every symbol has a duration $T = (2^{\mathrm{SF}}/B)$ and carries SF bits of information, where $\mathrm{SF} \in \{7, \ldots, 12\}$ is called the *SF*. For a symbol $s \in \{0, \ldots, 2^{\mathrm{SF}} - 1\}$, the signal starts at an initial frequency of $B([s/2^{\mathrm{SF}}] - [1/2])$. The instantaneous frequency of the modulated signal increases linearly over time, until

the moment $t_{\text{fold}} = [(2^{\text{SF}} - s)/B]$, when the instantaneous frequency is decreased by B (i.e., folded) to keep the signal in the allocated bandwidth [7]

$$x_s(t) = \begin{cases} e^{j2\pi\left(\frac{B}{2T_s}t^2 + B\left(\frac{s}{2^{\text{SF}}} - \frac{1}{2}\right)t\right)} & \text{for } 0 \le t < t_{\text{fold}} \\ e^{j2\pi\left(\frac{B}{2T_s}t^2 + B\left(\frac{s}{2^{\text{SF}}} - \frac{3}{2}\right)t\right)} & \text{for } t_{\text{fold}} \le t < T_s. \end{cases} \tag{1}$$

When sampled at the Nyquist frequency $f_s = B$, the discrete-time signal of a symbol consists of $N = 2^{\text{SF}}$ samples. The corresponding discrete-time baseband-equivalent model of a LoRa symbol s can be expressed as [6], [7]

$$x_s[n] = \begin{cases} e^{j2\pi\left(\frac{n^2}{2N} + \left(\frac{s}{N} - \frac{1}{2}\right)n\right)}, & 0 \le n < n_f \\ e^{j2\pi\left(\frac{n^2}{2N} + \left(\frac{s}{N} - \frac{3}{2}\right)n\right)}, & n_f \le n < N \end{cases} \tag{2}$$

where $n_f = N - s$ is the sample index at which the frequency folding occurs.

In this work, we assume that the transmission takes place over an additive white noise Gaussian (AWGN) channel with a complex-valued channel gain $h \in \mathbb{C}$. The received LoRa symbol is represented by

$$y[n] = hx_s[n] + z[n] \tag{3}$$

where $z[n] \sim \mathcal{CN}(0, \sigma^2)$ is complex AWGN with variance $\sigma^2 = (N_0/2)$ and N_0 is the single-sided noise power spectral density.

The ML detection of a LoRa symbol can be efficiently implemented at the Nyquist rate $f_s = B$ with a discrete Fourier transform (DFT). To this end, the sampled signal $y[n]$ is first multiplied pointwise with $x_0^*[n]$, the complex conjugate of an unmodulated symbol $s = 0$, which yields the *dechirped* signal

$$\tilde{y}[n] = y[n]x_0^*[n] = \sqrt{P}e^{j2\pi n\frac{s}{N} + \theta} + \tilde{z}[n] \tag{4}$$

where $P = |h|^2$ is the power of the signal at the receiver, $\theta = \angle h$ represents the phase introduced by the channel, and $\tilde{z}[n] = z[n]x_0^*[n]$. For a perfectly synchronized receiver, $\tilde{y}[n]$ contains a single complex tone of frequency (s/N) and AWGN. Let $Y[i] = \sum_{n=0}^{N-1} \tilde{y}[n]e^{-j2\pi(ni/N)}$ be the ith bin from the N-point DFT of the dechirped signal. In the frequency domain, the single complex tone of frequency (s/N) translates into a Kronecker delta at position $i = s$. LoRa receivers typically perform noncoherent ML detection by selecting the DFT bin with the largest magnitude [5]

$$\hat{s} = \arg\max_{\bar{s}} |Y[\bar{s}]|. \tag{5}$$

B. LoRa Preamble Structure

Every LoRa packet starts with a specific preamble for synchronization purposes. The preamble consists of N_{pr} repetitions of an unmodulated upchirp (i.e., $x_0[n]$), succeeded by two symbols acting as network identifiers, and 2.25 downchirps $x_0^*[n]$. The structure of the preamble is illustrated in Fig. 2.

It is well known that the combination of upchirps and downchirps can be exploited by a receiver to estimate the CFO and STO of a user [37], [38]. As explained in Section V-B, our two-user receiver also leverages this preamble in its synchronization stage.

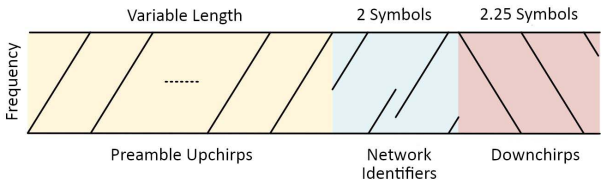

Fig. 2. Structure of a LoRa preamble.

C. Signal Model for Two Interfering Users

In this section, we describe the Nyquist-rate ($f_s = B$) model of superimposed signals from two users with the same SF, namely, user A and user B. Since LoRa uses a nonslotted ALOHA multiple access scheme, the users are neither synchronized among themselves nor to the gateway. Let us define $s_A^{(k)}$ and $s_B^{(k)}$ as the kth colliding symbols sent by users A and B, respectively. The symbols $s_A^{(1)}$ and $s_B^{(1)}$ are hence the two first information symbols of both users that collide with each other. To simplify the explanation and the mathematical formulation of the multiuser detector, we assume that the gateway is initially synchronized in frequency and time to user A, whose packet arrives first. This can be achieved with a standard synchronization procedure [37]–[39]. We define $\tau \in [0, N)$ as the relative sample-level time offset between the first sample of the kth symbol transmitted by user A and the first sample of the kth symbol of user B, as illustrated in Fig. 3. This sample offset can be split into an integer part $L_{\text{STO}} = \lfloor \tau \rfloor$ and a noninteger part $\lambda_{\text{STO}} = \tau - \lfloor \tau \rfloor$ [28].

Since the transmission of user B experiences an STO $\tau \ge 0$ with respect to user A, the first $\lfloor \tau \rfloor$ samples of symbol $s_A^{(k)}$ overlap with symbol $s_B^{(k-1)}$ and the last $N - \lfloor \tau \rfloor$ samples of symbol $s_A^{(k)}$ overlap with symbol $s_B^{(k)}$. The contribution of user B to the kth window of N samples $y^{(k)}[n]$ can therefore be split into two parts, namely, $y_{B,1}^{(k)}[n]$ for $n \in \mathcal{N}_1 = \{0, \ldots, \lceil \tau \rceil - 1\}$ and $y_{B,2}^{(k)}[n]$ for $n \in \mathcal{N}_2 = \{\lceil \tau \rceil, \ldots, N - 1\}$ [40], with

$$y_{B,1}^{(k)}[n] = e^{j2\pi\left(\frac{(n+N-\tau)^2}{2N} + (n+N-\tau)\left(\frac{s_B^{(k-1)}}{N} - \frac{1}{2} - u\left[n - n_{f,1}^{(k)}\right]\right)\right)} \tag{6}$$

$$y_{B,2}^{(k)}[n] = e^{j2\pi\left(\frac{(n-\tau)^2}{2N} + (n-\tau)\left(\frac{s_B^{(k)}}{N} - \frac{1}{2} - u\left[n - n_{f,2}^{(k)}\right]\right)\right)}. \tag{7}$$

Prior to synchronization, both users are affected by distinct CFOs relative to the receiver, namely, $\Delta f_{c,A}$ and $\Delta f_{c,B}$. However, since we assume the receiver to be synchronized to user A, there is only a single effective CFO $\Delta f_c = \Delta f_{c,B} - \Delta f_{c,A}$ that only affects the signal from user B. Similarly to the STO, the CFO can also be split into integer and fractional parts $L_{\text{CFO}} = \lfloor N(\Delta f_c/f_s) \rceil$ and $\lambda_{\text{CFO}} = N(\Delta f_c/f_s) - L_{\text{CFO}}$, where $\lfloor \cdot \rceil$ is the rounding operator [37]. Due to the low-cost crystal oscillators in LoRa transceivers, it is common to observe CFO values $L_{\text{STO}} + \lambda_{\text{CFO}}$ in the range $[-N/4, N/4]$ [38].

Finally, the users have different transmit powers and experience independent single-tap channels h_A and h_B. Let $P_A = |h_A|^2$ and $P_B = |h_B|^2$ be the received powers of users A and B, respectively, which we assume to be constant. However, since LoRa is intentionally designed for noncoherent detection [41], we do not make any assumption on the phase coherence of

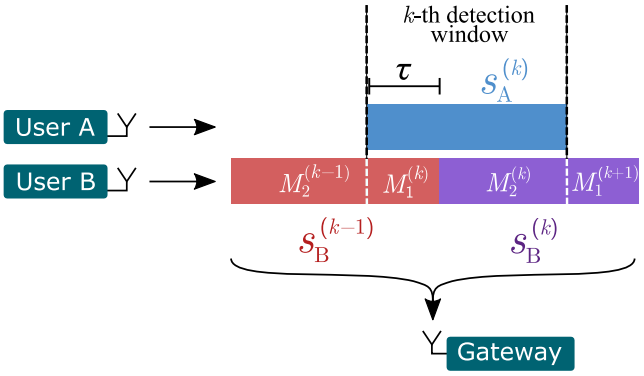

Fig. 3. Illustration of the matched filters outputs used by the detection of the overlapping symbols $s_A^{(k)}$, $s_B^{(k-1)}$, and $s_B^{(k)}$.

successive symbols. We thus define $\theta_A^{(k)}$ and $\theta_B^{(k)}$ as the initial phases of the kth symbol of user A and B, respectively. The discrete-time baseband-equivalent model of the received signal sampled at $f_s = B$ that represents the kth window of N samples is therefore

$$y^{(k)}[n] = \sqrt{P_A} e^{j\theta_A^{(k)}} x_{s_A^{(k)}}[n] + z[n] + \begin{cases} \sqrt{P_B} e^{j\theta_B^{(k-1)}} c[n] y_{B,1}^{(k)}[n], & n \in \mathcal{N}_1 \\ \sqrt{P_B} e^{j\theta_B^{(k)}} c[n] y_{B,2}^{(k)}[n], & n \in \mathcal{N}_2 \end{cases} \quad (8)$$

where $c[n] = e^{j2\pi n(\Delta f_c/f_s)}$ is the effective CFO affecting user B.

III. Practical ML-Derived Two-User Detector

In this section, we design a detector that is capable of jointly demodulating the symbols from two superimposed LoRa users. This detector is derived from the two-user MLSE, whose general structure is explained in [42]. We first derive the expression of the MLSE for the signal model defined in (8) and argue that its complexity is prohibitive in practice. To enable a practical implementation of the multiuser detector, we subsequently propose three simplifications to the two-user MLSE that notably reduce its complexity.

A. Two-User LoRa Maximum Likelihood Sequence Estimator

As previously explained, the two-user detector is only needed when the frames of two LoRa users overlap in time. The noncolliding parts of the frames can be demodulated with the single-user detector of (5), while only the colliding parts need to be processed with the two-user detector derived in this section. We note here that in the case of an overlap, the colliding part generally dominates the overall error rate. The proposed two-user detector uses as input the baseband signal $y^{(k)}[n]$ from (8), which is recovered with a single receiving antenna and sampled at the Nyquist frequency $f_s = B$. Let M be the number of symbols of user A colliding with symbols from user B. Following (8), the colliding parts of the frame can be decomposed into M successive windows of N samples. Similar to the single-user detector in (5), we propose to dechirp every window $y^{(k)}[n]$ with a reference downchirp $x_0^*[n]$ since the dechirped windows $\tilde{y}^{(k)}[n]$ possess a simpler analytical representation than $y^{(k)}[n]$ which facilitates the derivation of the ML detector.

In an AWGN channel, the MLSE seeks the sequence of symbols that minimizes the sum of the distances between the dechirped samples and the presumed contributions of each user [42]. Given the baseband model defined in (8), followed by the dechirping operation, the two-user MLSE seeks the set of candidate symbols $\bar{\boldsymbol{s}}^{(k)} = \{\bar{s}_A^{(k)}, \bar{s}_B^{(k-1)}, \bar{s}_B^{(k)}\} \in \{0, \ldots, N-1\}^3$ for $k \in \{0, \ldots, M-1\}$ maximizing the probability

$$p = C \exp\left(-\frac{1}{2\sigma^2} \left(\sum_{i=0}^{M-1} \sum_{n=0}^{N-1} \left\| \tilde{y}^{(i)}[n] - \tilde{x}^{(i)}\left[n | \bar{\boldsymbol{s}}^{(i)}\right] \right\|^2 \right) \right) \quad (10)$$

where $\tilde{x}^{(k)}[n|\boldsymbol{s}^{(k)}]$ represents the dechirped contributions of both users in the kth window and $C = (1/[\sqrt{2\pi\sigma^2}])^{MN}$. The expression of $\tilde{x}^{(k)}[n|\bar{\boldsymbol{s}}^{(k)}]$ is provided in (9), shown at the bottom of the page, and depends on the offsets Δf_c and τ, the phases $\{\theta_A^{(k)}, \theta_B^{(k-1)}, \theta_B^{(k)}\}$, and the received powers P_A and P_B of each user.

The ML sequence can be computed with reduced complexity using the Viterbi algorithm [42]. However, since there are N^2 possible states per window and N^3 possible state transitions between two windows, the complexity of this ML sequence detector is prohibitive, especially for large SFs (i.e., large N). In the remainder of this section, we propose three modifications that simplify the ML sequence detector of (10) to a more practical detector.

B. From Joint to Individual Maximum Likelihood Decisions

To avoid such a complex receiver, we suggest to move from a joint demodulation of all colliding symbols to individual decisions that are tied to windows of N samples. For each window k and the corresponding dechirped signal $\tilde{y}^{(k)}$, an individual decision amounts to detecting the overlapping symbols $\boldsymbol{s}^{(k)} = \{s_A^{(k)}, s_B^{(k-1)}, s_B^{(k)}\}$ as shown in Fig. 3. Let $\mathcal{L}(\bar{\boldsymbol{s}}^{(k)})$ denote the likelihood that the symbols $\bar{\boldsymbol{s}}^{(k)} = \{\bar{s}_A^{(k)}, \bar{s}_B^{(k-1)}, \bar{s}_B^{(k)}\}$ have been transmitted in the kth window

$$\mathcal{L}\left(\bar{\boldsymbol{s}}^{(k)}\right) = C \exp\left(-\frac{1}{2\sigma^2} \sum_{n=0}^{N-1} \left\| \tilde{y}^{(k)}[n] - \tilde{x}^{(k)}\left[n | \bar{\boldsymbol{s}}^{(k)}\right] \right\|^2 \right). \quad (11)$$

An individual ML decision for the kth window is obtained by selecting the symbols $\bar{\boldsymbol{s}}^{(k)}$ that maximize the likelihood $\mathcal{L}(\bar{\boldsymbol{s}}^{(k)})$. This likelihood can be expressed more intuitively after some

$$\tilde{x}^{(k)}\left[n|\boldsymbol{s}^{(k)}\right] = \begin{cases} \sqrt{P_A} e^{j\theta_A^{(k)}} e^{j2\pi \frac{n}{N} s_A^{(k)}} + \sqrt{P_B} e^{j\theta_B^{(k-1)} + 2\pi\lambda_{\mathrm{STO}} u\left[n - n_{f,1}^{(k)}\right]} \cdot e^{j2\pi \frac{(n+N-\tau)}{N}\left(s_B^{(k-1)} - \tau + N\frac{\Delta f_c}{f_s}\right)}, & n \in \mathcal{N}_1 \\ \sqrt{P_A} e^{j\theta_A^{(k)}} e^{j2\pi \frac{n}{N} s_A^{(k)}} + \sqrt{P_B} e^{j\theta_B^{(k)} + 2\pi\lambda_{\mathrm{STO}} u\left[n - n_{f,2}^{(k)}\right]} \cdot e^{j2\pi \frac{(n-\tau)}{N}\left(s_B^{(k)} - \tau + N\frac{\Delta f_c}{f_s}\right)}, & n \in \mathcal{N}_2 \end{cases} \quad (9)$$

with $n_{f,1}^{(k)} = \lceil \tau \rceil - s_B^{(k-1)}$ and $n_{f,2}^{(k)} = N + \lceil \tau \rceil - s_B^{(k)}$

simple algebraic transformations and after the removal of all constant factors. It is shown in the Appendix that maximizing the likelihood $\mathcal{L}(\bar{\boldsymbol{s}}^{(k)})$ amounts to maximizing the following metric:

$$\begin{aligned}\Lambda_{\mathrm{ML}}\left(\bar{\boldsymbol{s}}^{(k)}\right) = \exp\Big[&\sqrt{P_A}\Re\left(e^{-j\theta_A^{(k)}}Y^{(k)}\left[\bar{s}_A^{(k)}\right]\right)\\ &+\sqrt{P_B}\Re\left(e^{-j\theta_B^{(k-1)}}M_1^{(k)}\left[\bar{s}_A^{(k)},\bar{s}_B^{(k-1)}\right]\right)\\ &+\sqrt{P_B}\Re\left(e^{-j\theta_B^{(k)}}M_2^{(k)}\left[\bar{s}_A^{(k)},\bar{s}_B^{(k)}\right]\right)\Big] \quad (12)\end{aligned}$$

where $Y^{(k)}$, $M_1^{(k)}$, and $M_2^{(k)}$ correspond to three matched filters that are connected to the symbols $s_A^{(k)}$, $s_B^{(k-1)}$, and $s_B^{(k)}$, respectively. Each term of $\Lambda_{\mathrm{ML}}(\bar{\boldsymbol{s}}^{(k)})$ can be interpreted as a (partial) DFT matched to each one of the symbols contained in the window $y^{(k)}[n]$.

Since the receiver is synchronized to user A, the symbol $s_A^{(k)}$ translates to a Kronecker delta in the frequency domain. The matched filter $Y^{(k)}$ hence simply corresponds to the DFT of the entire dechirped signal $\tilde{y}^{(k)}[n]$

$$Y^{(k)}\left[\bar{s}_A^{(k)}\right] = \sum_{n=0}^{N-1}\tilde{y}^{(k)}[n]\cdot e^{-j2\pi\frac{n}{N}\bar{s}_A^{(k)}}. \quad (13)$$

The two remaining terms in (12) evaluate the contribution from user B, which is not synchronized. As the waveforms carrying the symbols $\bar{s}_B^{(k-1)}$ and $\bar{s}_B^{(k)}$ are modified from their original shape (i.e., a Kronecker delta) by the CFO and STO of user B, the individual ML detector uses two specific matched filters $M_1^{(k)}$ and $M_2^{(k)}$ which depend on the offsets Δf_c and τ. To detect both symbols, the individual ML detector eliminates the presumed contribution $\sqrt{P_A}e^{j\theta_A^{(k)}}e^{j2\pi(n/N)\bar{s}_A^{(k)}}$ of user A, corrects the CFO Δf_c and phase jump $2\pi\lambda_{\mathrm{STO}}$, and then computes a partial DFT over the first $\lceil\tau\rceil$ and the remaining $N-\lceil\tau\rceil$ samples in the window, respectively

$$\begin{aligned}M_1^{(k)}\left[\bar{s}_A^{(k)},\bar{s}_B^{(k-1)}\right] = &\sum_{n=0}^{\lceil\tau\rceil-1}\left(\tilde{y}^{(k)}[n]-\sqrt{P_A}e^{j\theta_A^{(k)}}e^{j2\pi\frac{n}{N}\bar{s}_A^{(k)}}\right)\\ &\cdot e^{-j2\pi\frac{(n+N-\tau)}{N}\left(\bar{s}_B^{(k-1)}-\tau+N\frac{\Delta f_c}{f_s}\right)}\\ &\cdot e^{-j2\pi\lambda_{\mathrm{STO}}u\left[n-n_{f,1}^{(k)}\right]}\end{aligned} \quad (14)$$

$$\begin{aligned}M_2^{(k)}\left[\bar{s}_A^{(k)},\bar{s}_B^{(k)}\right] = &\sum_{n=\lceil\tau\rceil}^{N-1}\left(\tilde{y}^{(k)}[n]-\sqrt{P_A}e^{j\theta_A^{(k)}}e^{j2\pi\frac{n}{N}\bar{s}_A^{(k)}}\right)\\ &\cdot e^{-j2\pi\frac{(n-\tau)}{N}\left(\bar{s}_B^{(k)}-\tau+N\frac{\Delta f_c}{f_s}\right)}\\ &\cdot e^{-j2\pi\lambda_{\mathrm{STO}}u\left[n-n_{f,2}^{(k)}\right]}.\end{aligned} \quad (15)$$

Yet, the matched filters $M_1^{(k)}$ and $M_2^{(k)}$ provide only partial information on the symbols $s_B^{(k-1)}$ and $s_B^{(k)}$. As illustrated in Fig. 3, the symbol $s_B^{(k-1)}$, in red, is connected to the matched filters $M_2^{(k-1)}$ and $M_1^{(k)}$, whereas the symbol $s_B^{(k)}$, in purple, is connected to the matched filters $M_2^{(k)}$ and $M_1^{(k+1)}$. Detecting these symbols using only the information from the kth window is clearly suboptimal. To efficiently demodulate the symbols $s_B^{(k-1)}$ and $s_B^{(k)}$, the detector must also use the partial information provided by the matched filters $M_2^{(k-1)}$ and $M_1^{(k+1)}$ of the preceding and the following windows, respectively. We hence suggest to first estimate $s_A^{(k)}$ by considering for every candidate symbol $\bar{s}_A^{(k)}$ the most likely symbols $\bar{s}_B^{(k-1)}$ and $\bar{s}_B^{(k)}$ independently of the previous and next windows as

$$\hat{s}_A^{(k)} = \arg\max_{\bar{s}_A^{(k)}}\max_{\bar{s}_B^{(k-1)},\bar{s}_B^{(k)}}\Lambda_{\mathrm{ML}}\left(\bar{s}_A^{(k)},\bar{s}_B^{(k-1)},\bar{s}_B^{(k)}\right). \quad (16)$$

We then decide on $s_B^{(k-1)}$ based on the prior decisions on $s_A^{(k-1)}$ and on the latest decision on $s_A^{(k)}$ as follows:

$$\hat{s}_B^{(k-1)} = \arg\max_{\bar{s}_B^{(k-1)}}\left|M_2^{(k-1)}\left[\hat{s}_A^{(k-1)},\bar{s}_B^{(k-1)}\right]+M_1^{(k)}\left[\hat{s}_A^{(k)},\bar{s}_B^{(k-1)}\right]\right|. \quad (17)$$

The decision on $s_B^{(k)}$ is deferred to the next time step. This rule requires that the receiver keeps in memory the vector containing the N matched filter outputs $M_2^{(k-1)}[\hat{s}_A^{(k-1)},\bar{s}_B^{(k-1)}]$ of the previous window.

C. Removing the Dependency on the Phases $\theta_A^{(k)}$ and $\theta_B^{(k)}$

The individual ML detection rules given in (16) and (17) require the knowledge of the phases $\theta_A^{(k)}$, $\theta_B^{(k-1)}$, and $\theta_B^{(k)}$. As previously mentioned, we do not assume that consecutive symbols of a user have identical phase offsets, i.e., we allow $\theta_A^{(k-1)} \neq \theta_A^{(k)}$. Although the phase of each user can theoretically be tracked over successive symbols, such a phase-tracking scheme notably increases the complexity of the receiver and its sensitivity to distortions. In this work, we propose instead to avoid this tracking and to remove the dependency on the phases by marginalizing over them in $\Lambda_{\mathrm{ML}}(\bar{\boldsymbol{s}}^{(k)})$.

First, the phases $\theta_B^{(k-1)}$ and $\theta_B^{(k)}$ can be easily marginalized over $[-\pi,\pi]$ [43], leading to a metric that relies on the magnitudes of $M_1^{(k)}$ and $M_2^{(k)}$

$$\begin{aligned}\Lambda'_{\mathrm{ML}}(\bar{\boldsymbol{s}}^{(k)}) &= \iint_{-\pi}^{\pi}\Lambda_{\mathrm{ML}}(\bar{\boldsymbol{s}}^{(k)})\,d\theta_B^{(k-1)}\,d\theta_B^{(k)}\\ &= \exp\left(\sqrt{P_A}\Re\left(e^{-j\theta_A^{(k)}}Y^{(k)}\left[\bar{s}_A^{(k)}\right]\right)\right)\\ &\quad\cdot I_0\left(\sqrt{P_B}\left|M_1^{(k)}\left[\bar{s}_A^{(k)},\bar{s}_B^{(k-1)}\right]\right|\right)\\ &\quad\cdot I_0\left(\sqrt{P_B}\left|M_2^{(k)}\left[\bar{s}_A^{(k)},\bar{s}_B^{(k)}\right]\right|\right)\end{aligned} \quad (18)$$

where $I_0(x)$ is the first-order-modified Bessel function of the first kind. This function is akin to e^x and has a practical closed-form expression. The only phase term remaining is $\theta_A^{(k)}$. Proper consideration of this phase is however more challenging, as it is used in all three terms of $\Lambda'_{\mathrm{ML}}(\bar{\boldsymbol{s}}^{(k)})$.

To lower the complexity of the integral over $\theta_A^{(k)}$, we propose to use an estimate of this phase in the matched filters $M_1^{(k)}$ and $M_2^{(k)}$. In a single-user scenario, the phase θ of a demodulated symbol $\hat{s}$ can be estimated by using the phase of the DFT bin $\hat{s}$, i.e., $\hat{\theta} = \arctan(Y[\hat{s}])$ [28]. We propose to use the same estimator with the DFT $Y^{(k)}$ to obtain an estimate $\hat{\theta}_A^{(k)}$ of the phase of the candidate symbol $\bar{s}_A^{(k)}$. Let $\widetilde{M}_1^{(k)}$ and $\widetilde{M}_2^{(k)}$ be modified versions of the filters $M_1^{(k)}$ and $M_2^{(k)}$ where the variable $\theta_A^{(k)}$ is replaced by the estimate $\hat{\theta}_A^{(k)}$ in the expression of the

matched filters $M_1^{(k)}$ and $M_2^{(k)}$. Also, let $\widetilde{\Lambda}(\bar{\boldsymbol{s}}^{(k)})$ be a modified version of the function $\Lambda'_{\mathrm{ML}}(\bar{\boldsymbol{s}}^{(k)})$, where the filters $\widetilde{M}_1^{(k)}$ and $\widetilde{M}_2^{(k)}$ are used instead of $M_1^{(k)}$ and $M_2^{(k)}$, respectively. A single occurrence of $\theta_A^{(k)}$ remains in $\widetilde{\Lambda}(\bar{\boldsymbol{s}}^{(k)})$, which is marginalized similarly to $\theta_B^{(k-1)}$ and $\theta_B^{(k)}$ to yield the final detection metric

$$\begin{aligned}\Lambda(\bar{\boldsymbol{s}}^{(k)}) &= \int_{-\pi}^{\pi} \widetilde{\Lambda}(\bar{\boldsymbol{s}}^{(k)})\, d\theta_A^{(k)} \\ &= I_0\Big(\sqrt{P_A}\Big|Y^{(k)}\Big(\bar{s}_A^{(k)}\Big)\Big|\Big) \\ &\quad \cdot I_0\Big(\sqrt{P_B}\Big|\widetilde{M}_1^{(k)}\Big(\bar{s}_A^{(k)}, \bar{s}_B^{(k-1)}\Big)\Big|\Big) \\ &\quad \cdot I_0\Big(\sqrt{P_B}\Big|\widetilde{M}_2^{(k)}\Big(\bar{s}_A^{(k)}, \bar{s}_B^{(k)}\Big)\Big|\Big). \end{aligned} \tag{19}$$

Due to the use of the nonideal estimate $\hat{\theta}_A^{(k)}$, the detector of (19) no longer follows the ML criterion. The accuracy of $\hat{\theta}_A^{(k)}$ depends not only on the noise level σ^2 but also on the contribution of user B that might overlap in the frequency domain with the symbol of user A. The accuracy of this approximation is therefore better when $P_A > P_B$, i.e., when the synchronized user is the strongest user. To maintain a decent interference cancelation in the matched filters $\widetilde{M}_1^{(k)}$ and $\widetilde{M}_2^{(k)}$, whose effectiveness strongly depends on the quality of the estimate $\hat{\theta}_A^{(k)}$, we assume in the remainder of this article that the receiver is always synchronized to the strongest user. In Section V, we show that the synchronization stage of a practical receiver can always take care of this requirement by allowing the receiver to resynchronize to an incoming user if that user has a higher received power than an active first user.

D. Pruning the Set of Candidate Symbols $\bar{s}_A^{(k)}$

Computing $\hat{s}_A^{(k)}$ with (16) requires to evaluate a significant number of metrics $\Lambda(\bar{\boldsymbol{s}}^{(k)})$. Per candidate symbol $\bar{s}_A^{(k)}$, N outputs for each of the matched filters $M_1^{(k)}$ and $M_2^{(k)}$ need to be evaluated. Since there are also N candidates for $\bar{s}_A^{(k)}$, the complexity for demodulating a window thus grows quadratically with N and becomes quickly prohibitive for large SFs. We previously explained that synchronizing to the strongest user improves the estimate $\hat{\theta}_A^{(k)}$. We now show that the synchronization to the strongest user can also be used to drastically reduce the complexity of the two-user detector.

According to (9), the contribution of user A to the dechirped signal $\tilde{y}^{(k)}[n]$ is a single complex tone of frequency $(s_A^{(k)}/N)$. On the contrary, the contribution of user B is no longer a single complex tone due to the effective CFO Δf_c and the STO τ. For the nonsynchronized user, the offset components L_{STO}, λ_{STO}, and λ_{CFO} scatter the energy of the symbols $s_B^{(k-1)}$ and $s_B^{(k)}$ over several frequency bins [40]. As illustrated in Fig. 4, the DFT of $\tilde{y}^{(k)}[n]$ contains a Kronecker delta corresponding to the symbol $s_A^{(k)}$, along with two bell-shaped functions centered around the frequencies

$$\frac{s_B^{(k-1)} - \tau + N\frac{\Delta f_c}{f_s}}{N} \text{ and } \frac{s_B^{(k)} - \tau + N\frac{\Delta f_c}{f_s}}{N}.$$

Both time and frequency offsets thus modify the spectral representation of the symbols from user B. We show in Section IV that the presence of an STO and a CFO between the users is actually beneficial to the performance of the two-user detector.

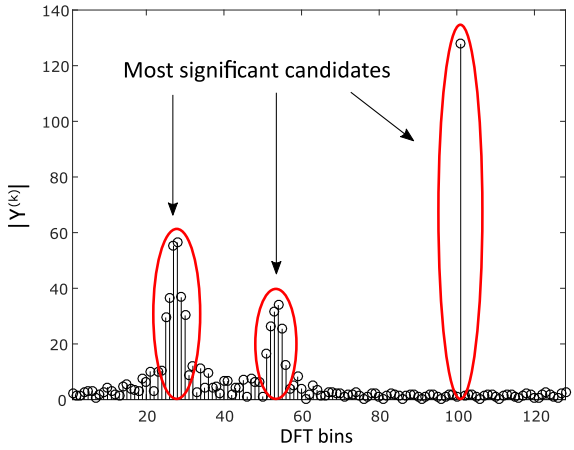

Fig. 4. Magnitude of the DFT $Y^{(k)}$ for $s_A^{(k)} = 100$, $s_B^{(k-1)} = 85$, $s_B^{(k)} = 59$, SF $= 7$, $\tau = 32.5$, $\Delta f_c = 0$, and $P_A = P_B$. Due to the STO τ, the symbols of user B are shifted in frequency and scattered on several DFT bins.

Since our receiver synchronizes to the strongest user, it is very likely at reasonable SNR levels that the DFT bin containing the symbol $s_A^{(k)}$ belongs to the limited set of bins with significant magnitudes. We therefore propose to reduce the complexity of (16) by selecting as candidates $\bar{s}_A^{(k)}$ only the K bins with the largest magnitudes $|Y^{(k)}(\bar{s}_A^{(k)})|$ among the N bins of the DFT $Y^{(k)}$. This rule reduces the total amount of matched filters $M_1^{(k)}$ and $M_2^{(k)}$ to evaluate per window from N^2 to KN.

The pruning of the set of candidate symbols $\bar{s}_A^{(k)}$ significantly reduces the complexity of the receiver. Per candidate symbol $\bar{s}_A^{(k)}$, N matched filter outputs $M_1^{(k)}[\bar{s}_A^{(k)}, \bar{s}_B^{(k-1)}]$ and $M_2^{(k)}[\bar{s}_A^{(k)}, \bar{s}_B^{(k)}]$ are evaluated, each requiring $\mathcal{O}(N)$ complex operations. Since the N outputs of the matched filter $Y^{(k)}$ can be computed in $\mathcal{O}(N \log N)$ operations using a fast Fourier transform, the computational complexity of the receiver is dominated by the evaluation of the matched filters $M_1^{(k)}$ and $M_2^{(k)}$. The demodulation of a window of N samples hence implies only $\mathcal{O}(KN^2)$ complex operations, compared to a complexity of $\mathcal{O}(N^3)$ without the pruning. We observed, in simulation trials, significant performance gains for $K = 2$ compared to $K = 1$, independently of the SF. Selecting $K > 5$ however does not further improve the performance for either user. In practical receivers, values of K between 2 and 5 should hence be used, depending on the available computational resources.

IV. Performance Evaluation of the Two-User Detector

In this section, we provide simulation results for the symbol error rate (SER) of both the stronger and the weaker colliding users using the detector derived in the previous section. The principal parameters that impact the SER are the STO τ between the users, the fractional part λ_{CFO} of the effective CFO, the difference $\Delta P = P_A - P_B$ of the received powers, and the SF. We analyze and discuss the impact of these parameters through Monte-Carlo simulations.

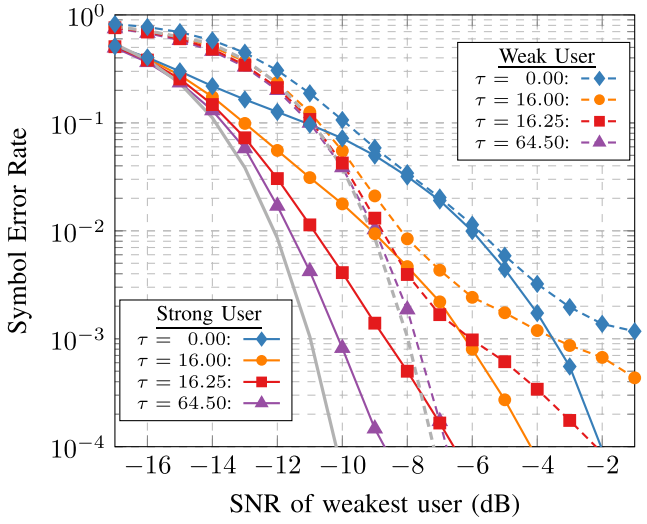

Fig. 5. SERs of both users for different values of τ with SF $= 7$, $\Delta f_c = 0$, and $\Delta P = 3$ dB. The thick gray lines show the SER for the noncoherent single-user receiver (5) in the absence of interference ($P_B = -\infty$ dB) [12].

The simulations are conducted in MATLAB as follows. For every trial, 10 000 collisions with overlapping payloads of $N_P = 32$ random LoRa symbols each are transmitted following the baseband model defined in (8). Since the length of LoRa payloads dominates over the preamble length, we only consider in this section collisions between two payloads. As Nyquist-frequency sampling is simulated, the signal bandwidth has no influence on the SERs. The transmitted symbols are demodulated using the detection rules (16) and (17) with the metric $\Lambda(\bar{s}^{(k)})$ from (19). The simulations in this section also assume perfect synchronization, i.e., the received power, CFO, and STO of each user are known. Results obtained without these idealized conditions and using a practical synchronization algorithm are presented in Section V. Furthermore, we use the simplification described in Section III and we choose the symbol candidates $\bar{s}_A^{(k)}$ for user A only from a limited set of the $K = 5$ most significant DFT bins. Unless specified otherwise, the following results are obtained for SF $= 7$. However, we show in Section IV-D that our detector benefits from the spreading gain of the LoRa modulation (about 2.5 dB per SF) in the same way as a single-user receiver. The results obtained for SF $= 7$ can hence serve as approximations for other SFs by appropriately subtracting the corresponding SNR offsets.

A. Impact of Sampling Time Offset

In Fig. 5, we compare four different scenarios for the STO for SF $= 7$, i.e., $N = 128$. In particular, we compare the worst case scenario with $\tau = 0.0$ (i.e., two users fully synchronized), the best case scenario with $\tau = 64.5$ (i.e., $\tau = N/2 + 0.5$), and two intermediate cases with $\tau = 16.0$ (i.e., $\tau = N/8$) and $\tau = 16.25$. The power difference between the two users is $\Delta P = 3$ dB. The SERs in the different scenarios are shown for both the strong and the weak user. The thick gray lines show the SER for the typical noncoherent single-user receiver (5) in the absence of interference. As expected, the performance with interference, both for the two-user and the multiuser receivers, is always worse than the no-interference case depicted by the gray lines. We note here that the two-user receiver demodulates the strongest user (solid curves) with error rates that are similar to the single-user detector in (5), but in the presence of interference. More interestingly, we observe that our two-user receiver allows even the weaker user (dashed curves) to be demodulated with useful SER values, while the typical single-user receiver would not be able to demodulate the weaker user at all.

We now discuss in detail the influence of the STO $\tau = L_{\text{STO}} + \lambda_{\text{STO}}$ on the demodulation. Considering first the impact of the integer offset L_{STO}, we clearly observe in Fig. 5 that a larger integer STO (up to $N/2$) reduces the SERs of both users. For the strongest user, the required SNR to attain a 10^{-3} SER, is 2.5 dB lower for $\tau = 16.0$ (solid orange curve) compared to $\tau = 0.0$ (solid purple curve). A similar behavior can be observed for the fractional part of the STO. We observe that a fractional STO (up to 0.5) can improve the error rate at ranges that are comparable to large integer values of STO and very close to the no-interference case. For example, the weakest user for $\tau = 16.25$ (i.e., $\lambda_{\text{STO}} = 0.25$, dashed red curve) reaches a SER of 10^{-3} at -6-dB SNR, whereas for $\tau = 16.0$ ($\lambda_{\text{STO}} = 0$, dashed orange curve), the required SNR is -4 dB.

The aforementioned observations indicate that the more the interfering users are desynchronized in time, the easier it is for the two-user receiver to separate and demodulate them. This effect can be explained by the contribution of each user to the DFT of the dechirped signal. While the contribution of the strongest and synchronized user is always a Kronecker delta, the spectral representation of the contribution of the weakest user depends on the STO τ. For $\tau = 0$, the symbols of both users are Kronecker deltas in the frequency domain and the matched filter $M_1^{(k)}$ is identical to the DFT $Y^{(k)}$. In such a time-aligned case, it is difficult to distinguish the symbols of the two users as they are entirely correlated to each other. In the presence of an STO $\tau \neq 0$, the contribution of the weakest user is no longer a single peak, but two bell-shaped functions scattered across several DFT bins, as introduced in Section III and observed in Fig. 4. Since the symbols of both users become less correlated in the presence of an STO, it is easier for the ML detector to separate the contribution of each user. Therefore, integer or fractional STOs close to $N/2$ or 0.5, respectively, significantly improve the performance of the proposed two-user detector. The extent of this behavior is also shown in Fig. 5, where, to demodulate the weakest user at a 10^{-3} SER, the best case scenario with $\tau = 64.5$ (dashed blue curve) requires a 7-dB lower SNR than the worst case scenario with $\tau = 0.0$ (dashed purple curve).

B. Impact of Carrier Frequency Offset

Similar to the STO, the effective CFO Δf_c between the users also modifies the spectral representation of the symbols sent by user B [28]. Yet, contrary to the STO, only the fractional part λ_{CFO} modifies the spectral representation of the symbols of user B. An integer CFO L_{STO} only shifts the symbols of user B by an integer number of DFT bins and, therefore, does not improve the detection performance.

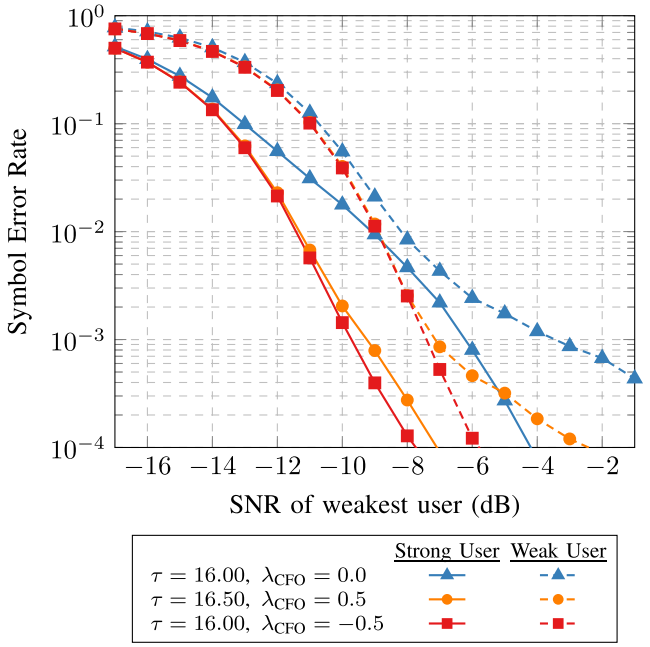

Fig. 6. SERs of both users for different values of τ and λ_{CFO} with SF $= 7$ and $\Delta P = 3$ dB.

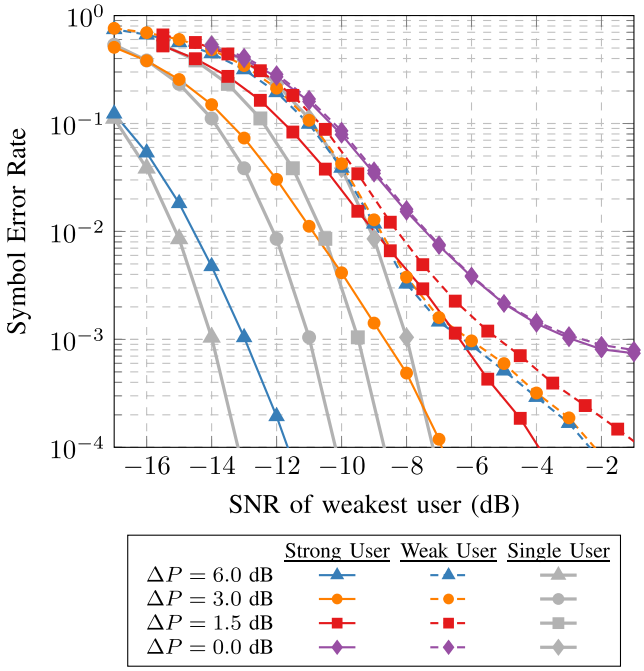

Fig. 7. SERs of both users for different values $\Delta P = P_A - P_B$ with SF $= 7$, $\tau = 16.25$, and $\Delta f_c = 0$. The thick gray lines show the SER of the single-user receiver (5) in the absence of interference ($P_B = -\infty$ dB) for the SNRs of the strong user.

The SERs for scenarios with SF $= 7$ and with different values of λ_{CFO} and λ_{STO} are presented in Fig. 6. Compared to the baseline $\lambda_{\text{CFO}} = 0.0$ with $\tau = 16.0$, an offset $\lambda_{\text{CFO}} = -0.5$ decreases the required SNR to attain a 10^{-3} SER by 3.5 dB for the strongest user. For the weakest user, the required SNR for the same SER is reduced by 3 dB. We note that previous works in the literature suggested that the fractional offsets λ_{STO} and λ_{CFO} modify the spectral representation of LoRa symbols in an identical way [37]. Yet, more recent analyses have shown that the contributions of the fractional STO and CFO, although similar, are not entirely equivalent [38], [40]. Compared to the CFO, the fractional STO additionally induces a phase jump of $2\pi\lambda_{\text{STO}}$ when the LoRa symbol folds in frequency, as modeled in (9). As a consequence, the performance of the detector depends on both values of λ_{STO} and λ_{CFO}, and is not only defined by the difference of the two $-\lambda_{\text{STO}} + \lambda_{\text{CFO}}$. This behavior is illustrated in Fig. 6 with the scenario $\lambda_{\text{CFO}} = 0.5$ and $\lambda_{\text{STO}} = 0.5$. Although the fractional offsets cancel each other in the term $s_B^{(k)} - \tau + N(f_c/f_s)$ of (9), the phase jump of $2\pi\lambda_{\text{STO}}$ still enables important performance gains for the two-user detector compared to the worst case fully time and frequency-aligned scenario.

C. Impact of the Received Powers Difference

We subsequently analyze the impact of the difference $\Delta P = P_A - P_B$ in the received powers of the colliding users. Fig. 7 shows the SERs of both the strong and the weak user for $\Delta P = 6$, 3, 1.5, and 0 dB, with SF $= 7$. We first discuss the effect of ΔP on the demodulation of the strongest user, and use the noncoherent single-user receiver in the absence of interference (5) as a reference. The results are presented for a fixed P_B, i.e., increasing ΔP amounts to increasing P_A. Hence, for the four values of ΔP studied, the baseline SER is inherently shifted horizontally by the corresponding increase of power P_A. For identical received powers ($\Delta P = 0$ dB), the SERs of both users become equivalent and level off near a SER of 10^{-3}. With $\Delta P = 1.5$ dB, the two-user detector reaches a SER value of 10^{-3} with an SNR of -6.5 dB, whereas the detector of (5) in a single-user scenario requires a 3-dB lower SNR for the same target. For $\Delta P = 3$ dB and $\Delta P = 6$ dB, the SNR difference between the two scenarios reduces to 2.5 and 1 dB, respectively. These results illustrate that, for an increasing ΔP, the SER of the strongest user converges to the SER of the no-interference case.

Interestingly, provided a small difference of received powers between the users, the value of ΔP itself does not significantly affect the error rates for the weakest user. We observe, for example, that the performance of the weak user for $\Delta P = 3$ dB and $\Delta P = 6$ dB is almost identical and similar to the case with $\Delta P = 1.5$ dB. The error rates however increase for $\Delta P = 0$ dB. The two-user detection rule (19) notably relies on the energy of the symbols to identify their corresponding user. When both users exhibit close received powers, the two-user detector is more likely to confuse their respective demodulated symbols. In this situation, the uncoded receiver is unable to correctly assign some demodulated symbol sequences to their respective users, even in high SNR regions.

Overall, the proposed two-user receiver yields useful SER values for the weak user when at least a small difference of received power ΔP exists. This observed behavior is a very positive result, since in typical single-user LoRa receivers, the weak user is always lost.

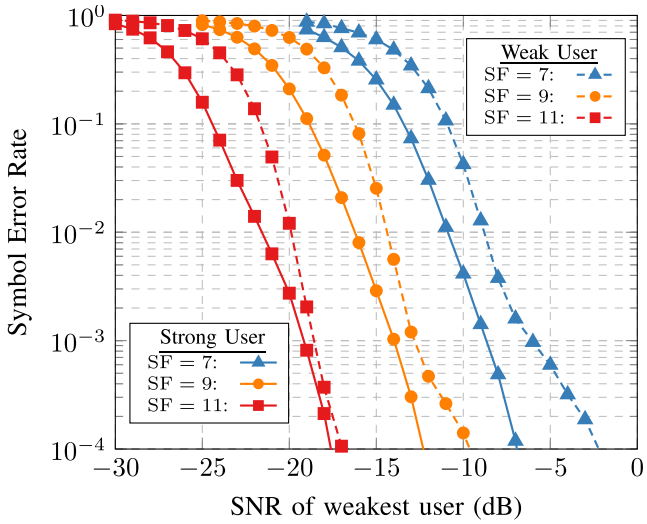

Fig. 8. SERs of both users for different SFs with $\Delta P = 3$ dB , $L_{\text{STO}} = N/8$, $\lambda_{\text{STO}} = 0.25$, and $\Delta f_c = 0$.

D. Impact of Different Spreading Factors

We finally discuss the impact of the SF on the performance of the two-user detector. Fig. 8 shows the SER of both the strong and weak users for three SFs SF = 7, 9, and 11. For the noncoherent single-user receiver (5), every increment of the SF by one enhances the spreading gain of the modulation by approximately 2.5 dB [28]. A similar behavior can be observed for the detection of the strongest user, as increasing the SF by two reduces the SNR requirements by approximately 5 dB for all SERs. Regarding the weakest user, the required SNR to attain a 10^{-3} SER when increasing the SF from 7 to 9 decreases by 7 dB. This 7-dB improvement not only stems from the increased spreading gain but also from more accurate estimates $\hat{\theta}_A^{(k)}$.

Since the number of different LoRa symbols $N = 2^{\text{SF}}$ increases with the SF, the probability that, during window k, symbol $s_A^{(k)}$ of the strong user overlaps in frequency with symbols $s_B^{(k-1)}$ or $s_B^{(k)}$ of the weak user also decreases. As a consequence, the phase estimator for $\hat{\theta}_A^{(k)}$ is less prone to suffer from interference coming from the weakest user. For SF = 7, an inflexion point in the error rate can be observed at a SER of $0.3 \cdot 10^{-2}$, i.e., for a -7-dB SNR. At lower SNR levels, the SER is dominated by errors due to noise, whereas for SNRs greater than -7 dB, the inaccuracies of the estimates $\hat{\theta}_A^{(k)}$ prevent the receiver from correctly removing the contribution of user A before detecting the symbols of user B. By increasing the SF to 9 and 11, this inflexion point drops to a SER of $0.9 \cdot 10^{-3}$ and $0.4 \cdot 10^{-3}$, respectively, and inaccurate estimates of $\hat{\theta}_A^{(k)}$ become less relevant.

V. Multiuser Synchronization Algorithm Robust To Interference

The two-user detector derived in Section III requires estimates of the received power, STO, and CFO of each user. To demonstrate the practicality of the proposed two-user detector in a full receiver chain, we present in this section an adaptive multiuser synchronization algorithm that is robust to the same-SF interference. Conventional single-user synchronization algorithms, e.g., [38], [39], and [44], are not capable of accurately estimating these parameters in the presence of interference from another user. Hence, a specific algorithm is needed. Compared to the synchronization procedures of the multiuser receivers from [30]–[35], our algorithm originally exploits the quasi-orthogonality between upchirps and downchirps in the LoRa preamble to estimate the parameters of an arriving user in spite of another ongoing, colliding transmission.

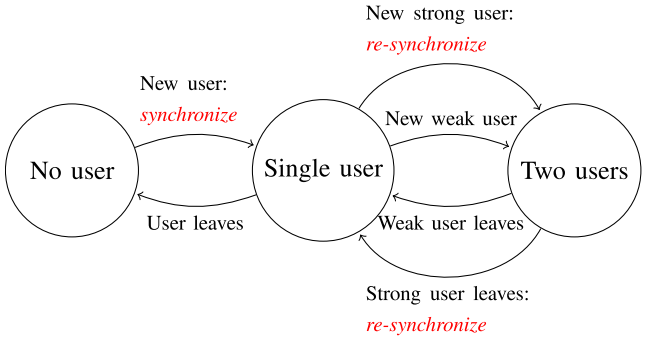

Fig. 9. FSM representation of the receiver. The receiver always synchronizes to the strongest user.

Both the two-user detector and the synchronization algorithm have been implemented in the GNU Radio software-defined radio environment. This C++ implementation is opensource and available at [45]. In the following, we first give an overview of the overall receiver architecture, and then explain the synchronization algorithm in detail. We then perform Monte-Carlo simulations with the GNU Radio implementation to evaluate the impact of the synchronization algorithm on the performance of the two-user detector. Finally, we briefly discuss the complexity of the proposed receiver.

A. Overview of the Synchronization Procedure

As previously explained, a LoRa user can start or stop transmitting at any time during the transmission of another user. Due to the nature of our two-user detector which demodulates simultaneously the symbols of two users, a gateway embedding this detector must be capable of tracking in real time the arrival of a second user during an ongoing transmission. To this end, the proposed multiuser synchronization algorithm implements a three-state finite-state machine (FSM) which is illustrated in Fig. 9. Each state corresponds to the current number of colliding users, up to two.

The input of the synchronization algorithm is an oversampled version $\bar{y}[n]$ of the received signal, sampled at the frequency $f_s' = RB$, where R is the oversampling factor. In the no-user or single-user states, the algorithm is constantly running to detect the preamble of a potential arriving user. When a new user is detected, the receiver estimates its power, CFO and STO using the oversampled received signal. In the presence of a single first user, the receiver synchronizes in time and frequency to this user. The synchronization comprises

finding the first sample of the payload in the oversampled signal $\bar{y}[n]$, decimating this signal by a factor R to the Nyquist frequency $f_s = B$, and correcting the estimated CFO, which finally yields the received signal $y[n]$. The typical noncoherent detector of (5) is then used to demodulate the payload symbols in $y[n]$.

Upon the arrival of a second user, the receiver switches to the two-user detection rules (16) and (17) that maximize the metric $\Lambda(\bar{s}^{(k)})$ from (19) with $K = 5$. If the new user has a higher received power than the active first user, the receiver resynchronizes in time and frequency to this new user. Maintaining the synchronization to the strongest user is an important condition to achieve decent interference cancelation in the two-user detector, as explained in Section III. The synchronized signal is split into windows of N samples, and each window is sent to the demodulation stage. Since the matched filters $M_1^{(k)}$ and $M_2^{(k)}$ require the knowledge of the effective CFO Δf_c and the STO τ, the synchronization algorithm is always ahead of the demodulation by $N_{\text{pr}} + 4.25$ symbols, i.e., the length of the preamble. This buffering enables the receiver to detect the new user and estimate its parameters before demodulating the interfering symbols of the already present user.

B. Estimation of the Parameters and Preamble Detection

Contrary to the algorithms of [38], [39], and [46], the synchronization algorithm of our two-user receiver has to detect and estimate the parameters of a new user even in the presence of a colliding user. For a single-user receiver, demodulating the upchirps and downchirps in the preamble (see Fig. 2) allows an unsynchronized receiver to estimate the integer parts of the CFO and STO [37]. In a noiseless environment, the symbols s_{up} and s_{down} of an upchirp and a downchirp demodulated with the single-user detector from (5) yield

$$\begin{aligned} s_{\text{up}} &= (L_{\text{CFO}} - L_{\text{STO}}) \bmod N \\ s_{\text{down}} &= (L_{\text{CFO}} + L_{\text{STO}}) \bmod N. \end{aligned} \tag{20}$$

The integer offsets L_{CFO} and L_{STO} are estimated by summing and subtracting s_{up} and s_{down}, respectively, and dividing the result by two. However, the conventional single-user detector is typically not able to correctly demodulate these symbols in the presence of strong interference. Hence, to perform a robust estimation of the CFO and STO, we propose instead to leverage the repetition of the upchirps as well as the almost orthogonal relationship between the 2.25 downchirps in the preamble of the second user and the modulated symbols of the first user [47].

The multiuser synchronization algorithm is divided into three stages. The first stage processes the upchirps of the preamble, the second processes the downchirps, and a final stage performs the preamble detection and the parameter estimation.

1) Estimation of s_{up} and λ_{CFO} Using the Upchirps: Due to the potential presence of interferers, it is not reliable to demodulate s_{up} with the single-user detector of (5). To estimate s_{up}, the proposed algorithm downsamples $\bar{y}[n]$ by a factor R, and distributes the decimated preamble signal into successive windows of N samples. Each window is then dechirped with the downchirp $x_0^*[n]$. Let $\bar{Y}^{(k)}$ be the DFT of the dechirped signal in the kth window. In the absence of interference, $\bar{Y}^{(k)}$ for an upchirp contains a single bell-shaped function centered around $s_{\text{up}} = (L_{\text{CFO}} - L_{\text{STO}}) \bmod N$ [38]. While a new user sends a preamble containing N_{pr} identical upchirps $x_0[n]$, it is highly likely that the payload symbols sent by the colliding same-SF user change over consecutive windows. We suggest to use the temporal repetition of the same upchirp in the preamble to filter out the time-varying symbols from an interfering user. In particular, we multiply the magnitudes of $\bar{Y}^{(k)}$ over $N_{\text{pr}} - 1$ consecutive windows and we perform the symbol decision on this product

$$\hat{s}_{\text{up}}^{(k)} = \arg\max_s \prod_{i=k}^{k+N_{\text{pr}}-1} \left|\bar{Y}^{(i)}[s]\right|. \tag{21}$$

The multiplication increases the magnitude of the frequency bins containing the identical symbols s_{up}, but it attenuates the energy of the payload symbols from the interfering users, which are located in different bins.

The preamble upchirps are then also used to estimate the fractional CFO λ_{CFO}. This offset can be estimated by multiplying the DFT bin $\bar{Y}^{(k)}[\hat{s}_{\text{up}}^{(k)}]$ with the complex conjugate of the same bin from the previous upchirp, and looking at the phase of the product [37]. In a two-user scenario, however, there is a nonnegligible probability that a symbol from the interferer overlaps in frequency with an upchirp of the new user, hence corrupting the estimate. We here reuse the estimator from [37]. However, to minimize the estimation errors due to noise or interference, we compute the estimate $\widehat{\lambda}_{\text{CFO}}^{(k)}$ over the same $N_{\text{pr}} - 1$ upchirps used to evaluate $\hat{s}_{\text{up}}^{(k)}$ with the preamble upchirps

$$\widehat{\lambda}_{\text{CFO}}^{(k)} = \frac{1}{2\pi} \arg\left(\sum_{i=k+1}^{k+N_{\text{pr}}-2} \bar{Y}^{(i)}\left[\hat{s}_{\text{up}}^{(k)}\right] \bar{Y}^{*(i-1)}\left[\hat{s}_{\text{up}}^{(k)}\right] \right). \tag{22}$$

2) Estimation of s_{down} and λ_{STO} Using the Downchirps: To estimate $s_{\text{down}} = (L_{\text{CFO}} + L_{\text{STO}}) \bmod N$ using the preamble downchirps, we suggest to perform a matched filter on the whole received preamble. When demodulating a LoRa symbol, a matched filter with N modulated downchirps is equivalent to the combination of the dechirping stage and the DFT stage. An oversampled matched filter however allows to simultaneously estimate the fractional time offset λ_{STO}.

The proposed filter $H^{(k)}$ looks for two consecutive unmodulated downchirps in the time windows $k-1$ and kth of RN samples each from the oversampled signal $\bar{y}[n]$. This filter also corrects for the fractional CFO, using the estimate $\widehat{\lambda}_{\text{CFO}}^{(k-N_{\text{pr}}-2)}$ obtained $N_{\text{pr}} - 2$ windows before

$$\begin{aligned} H^{(k)}[n,p] = \frac{1}{N} \sum_{m=0}^{2N-1} \bar{y}\big[R(Nk+m-n)-p\big] \\ \times \exp\left(j2\pi \left(\frac{m^2}{2N} - \frac{m}{2} - \frac{m}{N} \widehat{\lambda}_{\text{CFO}}^{(k-N_{pr}-2)} \right) \right) \end{aligned} \tag{23}$$

where $p \in \{0, \ldots, R-1\}$.

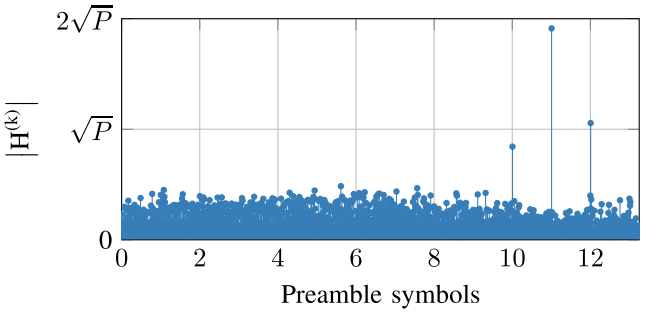

Fig. 10. Output of the matched filter $H^{(k)}$ on a received signal containing an entire preamble from a new user and random payload symbols from a 3-dB stronger interfering user with the same SF. The matched filter yields three distinct peaks of heights $\sqrt{P}$, $2\sqrt{P}$, and $\sqrt{P}$ spaced by RN samples when the downchirps of the preamble are processed. Conversely, the energy of the preamble upchirps and interfering payload symbols is spread through the whole filter output.

Let P be the received power of the arriving user. In the absence of interferers and noise, the filter reaches a maximum output magnitude of $2\sqrt{P}$ when it is aligned to the two downchirps. In this case, the peak at $2\sqrt{P}$ is attained for $n_{\max}^{(k)} = s_{\text{down}}$ and $p_{\max}^{(k)} = \lfloor R\lambda_{\text{STO}} \rceil$. Similarly, when only one downchirp is aligned, i.e., one window before or after the maximum at $2\sqrt{P}$, the magnitude of the output attains $\sqrt{P}$, for the same values of n and p. As the filter $H^{(k)}[n, p]$ is matched to downchirps, symbols from interferers, which are modulated with upchirps, are almost orthogonal and can hence be seen as AWGN [47]. This property is illustrated in Fig. 10.

3) Preamble Detection: The preamble detection is performed using the outputs $H^{(k)}[n, p]$ of the matched filter. The indices $n_{\max}^{(k)}$ and $p_{\max}^{(k)}$ of the largest absolute value of the matched filter output $|H^{(k)}[n, p]|$ are identified for each window. The algorithm detects a preamble when a succession of peaks of height $\sqrt{P}$, $2\sqrt{P}$, and $\sqrt{P}$ spaced by RN samples is observed, such that the following conditions are met:

$$\left| H^{(k-1)}\left[n_{\max}^{(k)}, p_{\max}^{(k)}\right] - \sqrt{\widehat{P}^{(k)}} \right| < T^{(k)} \tag{24}$$

$$\left| H^{(k+1)}\left[n_{\max}^{(k)}, p_{\max}^{(k)}\right] - \sqrt{\widehat{P}^{(k)}} \right| < T^{(k)} \tag{25}$$

where $T^{(k)} = \sqrt{\widehat{P}^{(k)} + (\sigma^2/N) + (2/\pi)}$ is a threshold that depends on the noise level and the SF, and $\widehat{P}^{(k)} = (0.5H^{(k)}[n_{\max}^{(k)}, p_{\max}^{(k)}])^2$ is the estimated received power.

Upon detection of a preamble, the symbols $\hat{s}_{\text{up}}^{(k-N_{\text{pr}}-2)}$ and $\hat{s}_{\text{down}}^{(k)} = n_{\max}^{(k)}$ are used to estimate L_{CFO} and L_{STO} following (20). The values $\widehat{\lambda}_{\text{STO}}^{(k)} = \lfloor (p_{\max}^{(k)}/R) \rceil$ and $\widehat{\lambda}_{\text{CFO}}^{(k-N_{\text{pr}}-2)}$ are selected as estimates of the fractional STO and CFO, respectively. It is worth noting that the proposed preamble detection rule is not guaranteed to work when the downchirps of two preambles collide, i.e., when the absolute time offset between the starts of the packets is smaller than 2.25 symbols. The probability that this scenario arises when two users collide is however negligible in practice, since the preamble is 12.25 symbols long and LoRaWAN frames carry at least 33 payload symbols for SF = 7 and 23 symbols for SF = 12 [2], [11].

C. Performance Evaluation

In the following, we evaluate in simulation the performance of our two-user detector when the parameters of the colliding users are estimated using the proposed multiuser synchronization algorithm. To analyze the performance of the two-user detector under nonideal, but realistic synchronization conditions, we first focus on the per-user SER when the receiver jointly demodulates two superimposed users after synchronizing with the proposed algorithm. The impact of the synchronization on the SERs is then further analyzed by studying the root mean square errors (RMSE) of the STO, the CFO, and the received power estimates.

The following results are obtained by simulating collisions in an AWGN channel between two LoRa transmitters using the GNU Radio software-defined-radio environment. In each Monte-Carlo trial, both transmitters send a LoRa packet with a preamble of 12.25 symbols and 32 random data symbols to the receiver. Seventy thousand trials are carried out per SNR level. To clearly illustrate the impact of the synchronization stage on the two-user detector, STO and CFO values that maximize the detection performance for both users have been chosen. The starting time of the transmission of the second user is delayed by 15 symbols and $\tau = 64.5$ samples with respect to the first user. The CFO between the two users is set such that $L_{\text{CFO}} + \lambda_{\text{CFO}} = 20.5$ and the transmit power of the second user is chosen 3 dB stronger than the power of the first user. AWGN is simulated at the receiver, and different SNR levels are obtained by sweeping the transmit powers of both users together. The receiver samples the received signal with an oversampling factor of $R = 8$. For the first user, only its payload symbols are subject to interference, whereas the colliding symbols of the second user comprise both preamble and payload symbols. Only the 15 overlapping payload symbols are used for the computation of the SERs. Trials in which the packet of the weakest user is not detected are not taken into account, as the two-user detector is not enabled in this scenario. For all simulated SNR levels and for both users, the probability of preamble misdetection is on average at least one order of magnitude smaller than the frame error rate.

Fig. 11 shows the SERs of both users with ideal synchronization and when the user parameters are estimated with the proposed multiuser synchronization algorithm. These SERs do not include the demodulation of the symbols that do not collide with another frame (i.e., the single-user state in the FSM of Fig. 9), since the proposed two-user detector is not used for these symbols that have an overall much lower SER. For a target SER of 10^{-3}, we observe for both users a loss of about 2 dB between the simulations with perfect synchronization and with our practical multiuser synchronization algorithm. To understand why this loss applies to both users, we show the RMSEs of the estimates of the fractional STO λ_{STO}, fractional CFO λ_{CFO}, and received power P of each user in Fig. 12. For all three parameters, the RMSEs of the first and second users are very similar, i.e., the estimates of the second user are not impaired by the presence of the other colliding user. In our simulations, the integer STO and CFO are always correctly estimated when the preamble is detected. Our synchronization

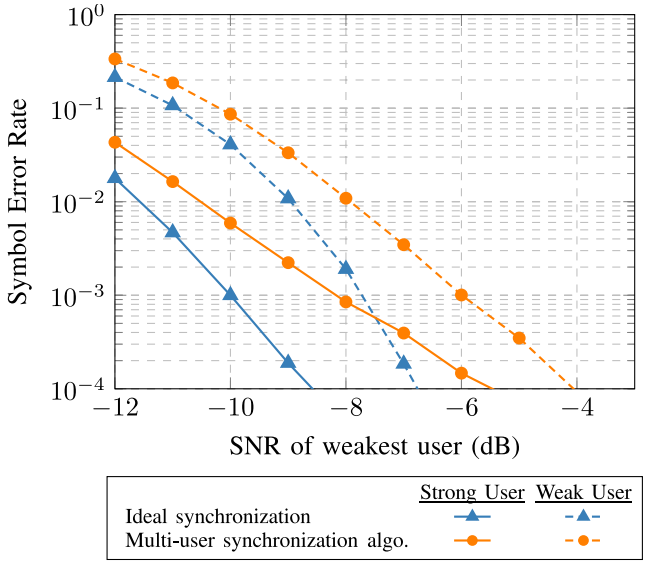

Fig. 11. SERs of both users for the proposed two-user detector with perfect synchronization and our multiuser synchronization algorithm for $\tau = 64.5$, $L_{\text{CFO}} = 20$, $\lambda_{\text{CFO}} = 0.5$, SF = 7, and $\Delta P = 3$ dB.

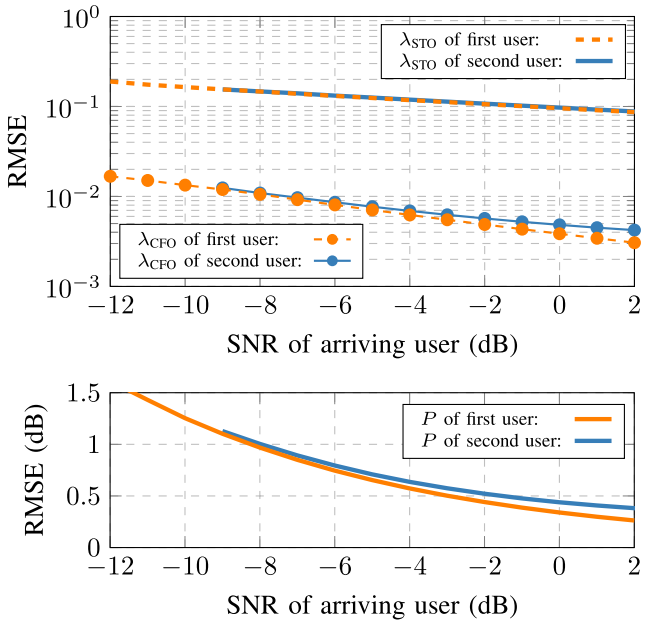

Fig. 12. RMSEs of the fractional STO, fractional CFO, and received power of each user for $R = 8$.

algorithm is hence robust to same-SF interferers, but induces a performance loss for the two-user detector.

The 2-dB loss is mainly due to the fractional STO, whose estimates are one order of magnitude less accurate than those of λ_{CFO}. The inaccuracy on λ_{STO} stems from the fact that our estimator relies on a matched filter with an oversampling factor R followed by a decision for the best match. As such, the resolution of the estimates $\widehat{\lambda}_{\text{STO}}^{(k)}$ is limited by R, even in the absence of noise. The estimation of the fractional CFO does not suffer from this limitation. We finally note that the estimator of the received power is biased as its RMSE floors at high SNR. This bias however does not strongly impact the two-user detector, since the SERs of both users decrease well below 10^{-4}.

D. Receiver Complexity Evaluation

We finally evaluate the complexity of the proposed two-user receiver, including the synchronization stage. Conventional single-user LoRa gateways use a single N-point FFT per symbol of N samples to carry out both the synchronization and the demodulation [48]. Assuming a Radix-2 FFT implementation, the processing of each input sample implies $(N/2)\log N$ complex multiplications. Our two-user detection rule requires, in addition to the FFT, the computation of KN outputs of the matched filters M_1 and M_2 per symbol, which amounts to KN complex multiply-and-accumulate (MAC) operations per sample. For SF = 7 and SF = 12, this overhead corresponds to 640 and 20 480 MACs per sample ($K = 5$), respectively, whereas the FFT requires 3.5 and 6 complex multiplications per sample. Similarly, the synchronization stage uses R parallel matched filters of length $2N$ on top of the FFT, which necessitate $2N$ additional MAC operations per sample (256 and 8192 MACs for SF = 7 and SF = 12, respectively). For the typical bandwidth and sampling frequency $B = f_s = 125$ kHz, the computational overhead of our receiver varies between $112 \cdot 10^6$ (SF = 7) and $3.5 \cdot 10^6$ (SF = 12) MACs per second. As a comparison, 5G NR mobile terminals carry out 4096-point FFTs with sampling rates up to $f_s = 122$ MHz [49], requiring $732 \cdot 10^6$ complex multiplications per second for a Radix-2 FFT.

VI. Conclusion

Multiuser receivers are required to overcome the scalability limitations of LoRa networks. In this article, we derived from the ML criterion a multiuser detector capable of demodulating symbols from two interfering LoRa users. The proposed detector inherently leverages the omnipresent differences in received power, time offsets, and frequency offsets to separate and demodulate the contribution of each user. For at least a 1.5-dB difference of the received power between the users, the detector is able to demodulate both users with useful error rates. To illustrate how this two-user detector may function in a practical receiver, we designed a synchronization algorithm that is robust to same-SF interference and implemented both blocks in the GNU Radio. In simulation, our GNU Radio implementation demodulates two colliding users with SERs below 10^{-3}, hence demonstrating the practicality of such a receiver.

Whereas conventional single-user LoRa receivers mainly rely on FFTs, our proposed two-user receiver uses matched filters with quadratic complexity for both the synchronization and detection stages and, therefore, requires more computing resources. However, thanks to the small bandwidths of LoRa signals, the overall complexity of the proposed gateway receiver remains similar to those of modern cellular terminals. In future works, we plan to conduct experiments with commercial LoRa devices to evaluate experimentally the potential benefits of the proposed solution at the network-level.

APPENDIX
DERIVATION OF THE JOINT MAXIMUM LIKELIHOOD DETECTOR

In this section, we show how the metric $\Lambda_{\mathrm{ML}}(\bar{\boldsymbol{s}}^{(k)})$ from (12) is derived from the likelihood expression given in (11). To simplify the derivations, we seek to maximize the log likelihood

$$\begin{aligned}\mathcal{L}'\left(\bar{\boldsymbol{s}}^{(k)}\right) &= \log \mathcal{L}(\bar{\boldsymbol{s}}^{(k)}) = A - \sum_{n=0}^{N-1}\left\|\tilde{y}^{(k)}[n] - \tilde{x}^{(k)}\left[n|\bar{\boldsymbol{s}}^{(k)}\right]\right\|^2 \\ &= \sum_{n=0}^{N-1}\Bigg[-\left\|\tilde{y}^{(k)}[n]\right\|^2 + 2\Re\left\{\tilde{y}^{(k)}[n]\tilde{x}^{(k)}\left[n|\bar{\boldsymbol{s}}^{(k)}\right]^*\right\} \\ &\quad - \left\|\tilde{x}^{(k)}\left[n|\bar{\boldsymbol{s}}^{(k)}\right]\right\|^2\Bigg] + A \end{aligned} \tag{26}$$

where A is a constant independent of $\bar{\boldsymbol{s}}^{(k)}$. We ignore, in the following developments, all terms that are independent of the candidate symbols $\bar{\boldsymbol{s}}^{(k)}$.

By developing $\tilde{x}^{(k)}[n|\bar{\boldsymbol{s}}^{(k)}]$ following (9), distributing all terms and using the relation $z_1 + z_1^* = 2\Re\{z_1\}$, we obtain:

$$\begin{aligned}\mathcal{L}'\left(\bar{\boldsymbol{s}}^{(k)}\right) &= \sum_{n=0}^{N-1} 2\Re\left(\tilde{y}^{(k)}[n]\cdot\sqrt{P_A}e^{-j\theta_A^{(k)}}e^{-j2\pi\frac{n}{N}\bar{s}_A^{(k)}}\right) \\ &\quad + \sum_{n=0}^{\lceil\tau\rceil-1} 2\Re\left(\tilde{y}^{(k)}[n]\cdot\sqrt{P_B}e^{-j\theta_B^{(k-1)}}\tilde{y}_{B,1}^{*(k)}[n]\right) \\ &\quad + \sum_{n=\lceil\tau\rceil}^{N-1} 2\Re\left(\tilde{y}^{(k)}[n]\cdot\sqrt{P_B}e^{-j\theta_B^{(k)}}\tilde{y}_{B,2}^{*(k)}[n]\right) \\ &\quad - \sum_{n=0}^{\lceil\tau\rceil-1} 2\Re\left(\sqrt{P_AP_B}e^{j\left(\theta_A^{(k)}-\theta_B^{(k-1)}\right)}e^{j2\pi\frac{n}{N}\bar{s}_A^{(k)}}\tilde{y}_{B,1}^{*(k)}[n]\right) \\ &\quad - \sum_{n=\lceil\tau\rceil}^{N-1} 2\Re\left(\sqrt{P_AP_B}e^{j\left(\theta_A^{(k)}-\theta_B^{(k)}\right)}e^{j2\pi\frac{n}{N}\bar{s}_A^{(k)}}\tilde{y}_{B,2}^{*(k)}[n]\right) \\ &\quad - N(P_A+P_B)\end{aligned} \tag{27}$$

where $\tilde{y}_{B,1}^{(k)}[n]$ and $\tilde{y}_{B,2}^{(k)}[n]$ represent the dechirped signals of the candidate symbols of user B in the kth window

$$\tilde{y}_{B,1}^{(k)}[n] = e^{j2\pi\frac{(n+N-\tau)}{N}\left(\bar{s}_B^{(k-1)}-\tau+N\frac{\Delta f_c}{f_s}\right)}e^{j2\pi\lambda_{\mathrm{STO}}u\left[n-n_{f,1}^{(k)}\right]} \tag{28}$$

$$\tilde{y}_{B,2}^{(k)}[n] = e^{j2\pi\frac{(n-\tau)}{N}\left(\bar{s}_B^{(k)}-\tau+N\frac{\Delta f_c}{f_s}\right)}e^{j2\pi\lambda_{\mathrm{STO}}u\left[n-n_{f,2}^{(k)}\right]}. \tag{29}$$

After dividing $\mathcal{L}'(\bar{\boldsymbol{s}}^{(k)})$ by two, removing the constant term $N(P_A+P_B)$ and by grouping the terms containing $\tilde{y}_{B,1}^{(k)}[n]$ or $\tilde{y}_{B,2}^{(k)}[n]$ together, the log likelihood becomes

$$\begin{aligned}\mathcal{L}'\left(\bar{\boldsymbol{s}}^{(k)}\right) &= \sum_{n=0}^{N-1}\Re\left(\sqrt{P_A}e^{-j\theta_A^{(k)}}\tilde{y}^{(k)}[n]e^{-j2\pi\frac{n}{N}\bar{s}_A^{(k)}}\right) \\ &\quad + \sum_{n=0}^{\lceil\tau\rceil-1}\Re\left[\tilde{y}_{\mathrm{IC}}^{(k)}[n]\sqrt{P_B}e^{-j\theta_B^{(k-1)}}\tilde{y}_{B,1}^{*(k)}[n]\right] \\ &\quad + \sum_{n=\lceil\tau\rceil}^{N-1}\Re\left[\tilde{y}_{\mathrm{IC}}^{(k)}[n]\sqrt{P_B}e^{-j\theta_B^{(k)}}\tilde{y}_{B,2}^{*(k)}[n]\right]\end{aligned} \tag{30}$$

where $\tilde{y}_{\mathrm{IC}}^{(k)}[n] = \tilde{y}^{(k)}[n] - \sqrt{P_A}e^{j\theta_A^{(k)}}e^{j2\pi(n/N)\bar{s}_A^{(k)}}$ is the interference-canceled version of $\tilde{y}^{(k)}[n]$, i.e., the dechirped received signal with the presumed contribution of user A removed.

Each term of (30) corresponds to a matched filtering of one of the symbols $\bar{s}_A^{(k)}$, $\bar{s}_B^{(k-1)}$, and $\bar{s}_B^{(k)}$ in the window. To ease the writing of $\mathcal{L}'(\bar{\boldsymbol{s}}^{(k)})$, we substitute in (30) the expressions of the matched filters $Y^{(k)}$, $M_1^{(k)}$, and $M_2^{(k)}$ defined in Section III

$$\begin{aligned}\mathcal{L}'\left(\bar{\boldsymbol{s}}^{(k)}\right) &= \sqrt{P_A}\Re\left(e^{-j\theta_A^{(k)}}Y^{(k)}\left[\bar{s}_A^{(k)}\right]\right) \\ &\quad + \sqrt{P_B}\Re\left(e^{-j\theta_B^{(k-1)}}M_1^{(k)}\left[\bar{s}_A^{(k)},\bar{s}_B^{(k-1)}\right]\right) \\ &\quad + \sqrt{P_B}\Re\left(e^{-j\theta_B^{(k)}}M_2^{(k)}\left[\bar{s}_A^{(k)},\bar{s}_B^{(k)}\right]\right).\end{aligned} \tag{31}$$

The metric $\Lambda_{\mathrm{ML}}(\bar{\boldsymbol{s}}^{(k)})$ subject to maximization is finally obtained from (31) by adding back the exponential function.

REFERENCES

[1] U. Raza, P. Kulkarni, and M. Sooriyabandara, "Low power wide area networks: An overview," *IEEE Commun. Surveys Tuts.*, vol. 19, no. 2, pp. 855–873, 2nd Quart., 2017.

[2] J. Haxhibeqiri, E. De Poorter, I. Moerman, and J. Hoebeke, "A survey of LoRaWAN for IoT: From technology to application," *Sensors*, vol. 18, no. 11, p. 3995, 2018.

[3] K. Mekki, E. Bajic, F. Chaxel, and F. Meyer, "A comparative study of LPWAN technologies for large-scale IoT deployment," *ICT Exp.*, vol. 5, no. 1, pp. 1–7, 2019.

[4] A. Augustin, J. Yi, T. Clausen, and W. M. Townsley, "A study of LoRa: Long range & low power networks for the Internet of Things," *Sensors*, vol. 16, no. 9, p. 1466, 2016.

[5] L. Vangelista, "Frequency shift chirp modulation: The LoRa modulation," *IEEE Signal Process. Lett.*, vol. 24, no. 12, pp. 1818–1821, Dec. 2017.

[6] R. Ghanaatian, O. Afisiadis, M. Cotting, and A. Burg, "LoRa digital receiver analysis and implementation," in *Proc. IEEE Int. Conf. Acoust. Speech Signal Process. (ICASSP)*, 2019, pp. 1498–1502.

[7] M. Chiani and A. Elzanaty, "On the LoRa modulation for IoT: Waveform properties and spectral analysis," *IEEE Internet Things J.*, vol. 6, no. 5, pp. 8463–8470, Oct. 2019.

[8] G. Baruffa, L. Rugini, L. Germani, and F. Frescura, "Error probability performance of chirp modulation in uncoded and coded LoRa systems," *Digit. Signal Process.*, vol. 106, Nov. 2020, Art. no. 102828.

[9] Y. Guo and Z. Liu, "Time-delay-estimation-liked detection algorithm for LoRa signals over multipath channels," *IEEE Wireless Commun. Lett.*, vol. 9, no. 7, pp. 1093–1096, Jul. 2020.

[10] N. BniLam, D. Joosens, M. Aernouts, J. Steckel, and M. Weyn, "LoRay: AoA estimation system for long range communication networks," *IEEE Trans. Wireless Commun.*, vol. 20, no. 3, pp. 2005–2018, Mar. 2021.

[11] "LoRaWAN specification v1.1." 2017. [Online]. Available: https://lora-alliance.org/resource_hub/lorawan-specification-v1-1/

[12] T. Elshabrawy and J. Robert, "Closed-form approximation of LoRa modulation BER performance," *IEEE Commun. Lett.*, vol. 22, no. 9, pp. 1778–1781, Sep. 2018.

[13] J. Petäjäjärvi, K. Mikhaylov, M. Pettissalo, J. Janhunen, and J. Iinatti, "Performance of a low-power wide-area network based on LoRa technology: Doppler robustness, scalability, and coverage," *Int. J. Distrib. Sensor Netw.*, vol. 13, no. 3, pp. 1–16, 2017.

[14] J. C. Liando, A. Gamage, A. W. Tengourtius, and M. Li, "Known and unknown facts of LoRa: Experiences from a large-scale measurement study," *ACM Trans. Sensor Netw.*, vol. 15, no. 2, pp. 1–35, 2019.

[15] D. Magrin, M. Centenaro, and L. Vangelista, "Performance evaluation of LoRa networks in a smart city scenario," in *Proc. IEEE Int. Conf. Commun. (ICC)*, 2017, pp. 1–7.

[16] O. Georgiou and U. Raza, "Low power wide area network analysis: Can LoRa scale?" *IEEE Wireless Commun. Lett.*, vol. 6, no. 2, pp. 162–165, Apr. 2017.

[17] M. C. Bor, U. Roedig, T. Voigt, and J. M. Alonso, "Do LoRa low-power wide-area networks scale?" in *Proc. 19th ACM Int. Conf. Model. Anal. Simulat. Wireless Mobile Syst.*, 2016, pp. 59–67.

[18] J. Haxhibeqiri, F. Van den Abeele, I. Moerman, and J. Hoebeke, "LoRa scalability: A simulation model based on interference measurements," *Sensors*, vol. 17, no. 6, p. 1193, 2017.
[19] D. Magrin, M. Capuzzo, and A. Zanella, "A thorough study of LoRaWAN performance under different parameter settings," *IEEE Internet Things J.*, vol. 7, no. 1, pp. 116–127, Jan. 2020.
[20] T. Polonelli, D. Brunelli, A. Marzocchi, and L. Benini, "Slotted ALOHA on LoRaWAN—Design, analysis, and deployment," *Sensors*, vol. 19, no. 4, p. 838, Feb. 2019.
[21] J. Haxhibeqiri, I. Moerman, and J. Hoebeke, "Low overhead scheduling of LoRa transmissions for improved scalability," *IEEE Internet Things J.*, vol. 6, no. 2, pp. 3097–3109, Apr. 2019.
[22] B. Reynders, Q. Wang, P. Tuset-Peiro, X. Vilajosana, and S. Pollin, "Improving reliability and scalability of LoRaWANs through lightweight scheduling," *IEEE Internet Things J.*, vol. 5, no. 3, pp. 1830–1842, Jun. 2018.
[23] Z. Xu, J. Luo, Z. Yin, T. He, and F. Dong, "S-MAC: Achieving high scalability via adaptive scheduling in LPWAN," in *Proc. IEEE INFOCOM Conf. Comput. Commun.*, 2020, pp. 506–515.
[24] A. Gamage, J. C. Liando, C. Gu, R. Tan, and M. Li, "LMAC: Efficient carrier-sense multiple access for LoRa," in *Proc. 26th Annu. Int. Conf. Mobile Comput. Netw. (MobiCom)*, Sep. 2020, pp. 1–13.
[25] I. Arun and T. Venkatesh, "Order statistics based analysis of pure ALOHA in channels with multipacket reception," *IEEE Commun. Lett.*, vol. 17, no. 10, pp. 2012–2015, Oct. 2013.
[26] D. Croce, M. Gucciardo, S. Mangione, G. Santaromita, and I. Tinnirello, "Impact of LoRa imperfect orthogonality: Analysis of link-level performance," *IEEE Commun. Lett.*, vol. 22, no. 4, pp. 796–799, Apr. 2018.
[27] O. Afisiadis, M. Cotting, A. Burg, and A. Balatsoukas-Stimming, "LoRa symbol error rate under non-aligned interference," in *Proc. IEEE Asilomar Conf. Signals Syst. Comput.*, Nov. 2019, pp. 1957–1961.
[28] O. Afisiadis, M. Cotting, A. Burg, and A. Balatsoukas-Stimming, "On the error rate of the LoRa modulation with interference," *IEEE Trans. Wireless Commun.*, vol. 19, no. 2, pp. 1292–1304, Feb. 2020.
[29] R. Fernandes, R. Oliveira, M. Luís, and S. Sargento, "On the real capacity of LoRa networks: The impact of non-destructive communications," *IEEE Commun. Lett.*, vol. 23, no. 12, pp. 2437–2441, Dec. 2019.
[30] M. A. B. Temim, G. Ferré, B. Laporte-Fauret, D. Dallet, B. Minger, and L. Fuché, "An enhanced receiver to decode superposed LoRa-like signals," *IEEE Internet Things J.*, vol. 7, no. 8, pp. 7419–7431, Aug. 2020.
[31] S. Tong, J. Wang, and Y. Liu, "Combating packet collisions using non-stationary signal scaling in LPWANs," in *Proc. 18th Int. Conf. Mobile Syst. Appl. Services*, 2020, pp. 234–246.
[32] B. Hu, Z. Yin, S. Wang, Z. Xu, and T. He, "SCLoRa: Leveraging multi-dimensionality in decoding collided LoRa transmissions," in *Proc. IEEE 28th Int. Conf. Netw. Protocols*, 2020, pp. 1–11.
[33] X. Xia, Y. Zheng, and T. Gu, "FTrack: Parallel decoding for LoRa transmissions," : *IEEE/ACM Trans. Netw.*, vol. 28, no. 6, pp. 2573–2586, Dec. 2020.
[34] S. Tong, Z. Xu, and J. Wang, "CoLora: Enabling multi-packet reception in LoRa," in *Proc. IEEE INFOCOM Conf. Comput. Commun.*, 2020, pp. 2303–2311.
[35] M. O. Shahid, M. Philipose, K. Chintalapudi, S. Banerjee, and B. Krishnaswamy, "Concurrent interference cancellation: Decoding multi-packet collisions in LoRa," in *Proc. ACM SIGCOMM Conf.*, 2021, pp. 503–515.
[36] M. Xhonneux, J. Tapparel, O. Afisiadis, A. Balatsoukas-Stimming, and A. Burg, "A maximum-likelihood-based multi-user LoRa receiver implemented in GNU radio," in *Proc. IEEE 54th Asilomar Conf. Signals Syst. Comput.*, 2020, pp. 1106–1111.
[37] C. Bernier, F. Dehmas, and N. Deparis, "Low complexity LoRa frame synchronization for ultra-low power software-defined radios," *IEEE Trans. Commun.*, vol. 68, no. 5, pp. 3140–3152, May 2020.
[38] M. Xhonneux, O. Afisiadis, D. Bol, and J. Louveaux, "A low-complexity LoRa Synchronization algorithm robust to sampling time offsets," *IEEE Internet Things J.*, vol. 9, no. 5, pp. 3756–3769, Mar. 2022.
[39] J. Tapparel, O. Afisiadis, P. Mayoraz, A. Balatsoukas-Stimming, and A. Burg, "An open-source LoRa physical layer prototype on GNU radio," in *Proc. IEEE Int. Workshop Signal Process. Adv. Wireless Commun. (SPAWC)*, 2020, pp. 1–5.
[40] O. Afisiadis, S. Li, J. Tapparel, A. Burg, and A. Balatsoukas-Stimming, "On the advantage of coherent LoRa detection in the presence of interference," *IEEE Internet Things J.*, vol. 8, no. 4, pp. 11581–11593, Jul. 2021.
[41] O. Seller and N. Sornin, "Low complexity, low power and long range radio receiver," U.S. Patent Appl. 15 620 364, Jan.–Apr. 2018.
[42] S. Verdu, "Optimum multiuser detection," in *Multiuser Detection*. Cambridge, U.K.: Cambridge Univ. Press, 1998, ch. 4, pp. 154–233.
[43] J. Proakis and M. Salehi, "Optimum receivers for AWGN channels," in *Digital Communications*. New York, NY, USA: McGraw-Hill, 2008, ch. 4, pp. 160–289.
[44] T. Ameloot, H. Rogier, M. Moeneclaey, and P. Van Torre, "LoRa signal Synchronization and detection at extremely low signal-to-noise ratios," *IEEE Internet Things J.*, vol. 9, no. 11, pp. 8869–8882, Jun. 2022.
[45] "Multi-user LoRa repository." [Online]. Available: https://www.epfl.ch/labs/tcl/resources-and-sw/lora-multi-user-receiver/ (Accessed: Dec. 7, 2020).
[46] V. Savaux, C. Delacourt, and P. Savelli. "On time-frequency Synchronization in LoRa system: From analysis to near-optimal algorithm." Jan. 2021. doi: 10.36227/techrxiv.13560158.v1.
[47] Z. Xu, S. Tong, P. Xie, and J. Wang, "FlipLoRa: Resolving collisions with up-down quasi-orthogonality," in *Proc. 17th Annu. IEEE Int. Conf. Sens. Commun. Netw.*, Jun. 2020, pp. 1–9.
[48] O. Seller and C. Devaucelle, "LoRa advanced receiver," U.S. Patent Appl. 20 210 184 901, Jul. 2021.
[49] H. Kim, "Design principles for 5G communications and networks," in *Design and Optimization for 5G Wireless Communications*. Hoboken, NJ, USA: Wiley, 2020, ch. 6, pp. 197–238.

Mathieu Xhonneux (Graduate Student Member, IEEE) received the M.Sc. degree in electrical engineering from the Université catholique de Louvain, Louvain-la-Neuve, Belgium, in 2018, where he is currently pursuing the Ph.D. degree in engineering science.

His current research interests include hardware/software codesign of signal processing systems and wireless communications for Internet of Things.

Joachim Tapparel received the B.Sc. and M.Sc. degrees in electrical engineering from the École Polytechnique Fédérale de Lausanne, Lausanne, Switzerland, in 2018 and 2021, respectively, where he is currently pursuing the Ph.D. degree with the Telecommunications Circuits Laboratory.

His research interests include wireless communications for Internet of Things systems, digital signal processing for communications, and interference mitigation in communications.

Alexios Balatsoukas-Stimming (Member, IEEE) received the Diploma and M.Sc. degrees in electronics and computer engineering from the Technical University of Crete, Chania, Greece, in 2010 and 2012, respectively, and the Ph.D. degree in computer and communications sciences from the École Polytechnique Fédérale de Lausanne (EPFL), Lausanne, Switzerland, in 2016.

He was a Marie SklodowskaCurie Postdoctoral Fellow with the European Laboratory for Particle Physics, Meyrin, Switzerland, for one year. He was a Postdoctoral Researcher with the Telecommunications Circuits Laboratory, EPFL from 2018 to 2019. He has also been a Visiting Postdoctoral Researcher with Cornell University, Ithaca, NY, USA, and the University of California at Irvine, Irvine, CA, USA. He is currently an Assistant Professor with the Department of Electrical Engineering, Eindhoven University of Technology, Eindhoven, The Netherlands. His research interests include VLSI circuits for communications, error correction coding theory and practice, and applications of approximate computing and machine learning to signal processing for communications.

Andreas Burg (Senior Member, IEEE) was born in Munich, Germany, in 1975. He received the Dipl.-Ing. degree from the Swiss Federal Institute of Technology (ETH) Zurich, Zurich, Switzerland, in 2000, and the Dr.Sc.Techn. degree from the Integrated Systems Laboratory, ETH Zurich, in 2006.

He worked with Siemens Semiconductors, San Jose, CA, USA, in 1998. During his doctoral studies, he worked with the Bell Labs Wireless Research, Holmdel, NJ, USA, for a total of one year. He was a Postdoctoral Researcher with the Integrated Systems Laboratory and the Communication Theory Group, ETH Zurich, from 2006 to 2007. He co-founded Celestrius, an ETH-spinoff in the field of MIMO wireless communication, in 2007, where he was responsible for the ASIC development as the Director of VLSI. In January 2009, he joined ETH Zurich as the SNF Assistant Professor and the Head of the Signal Processing Circuits and Systems Group, Integrated Systems Laboratory. In January 2011, he joined the École Polytechnique Fédérale de Lausanne, Lausanne, Switzerland, where he is leading the Telecommunications Circuits Laboratory. He was promoted to an Associate Professor with Tenure in June 2018.

Dr. Burg has served for the TPC of various conferences on signal processing, communications, and VLSI. He was a TPC Co-Chair of VLSI-SoC 2012, ESSCIRC 2016, and SiPS 2017. He was a General Chair of ISLPED 2019 and he served as an Editor for the IEEE TRANSACTION OF CIRCUITS AND SYSTEMS in 2013 and for the editorial board of the *Microelectronics Journal* (Springer). He is currently the Editor of the *Journal on Signal Processing Systems* (Springer), *MDPI Journal on Low Power Electronics and Its Applications*, IEEE TRANSACTIONS ON VERY LARGE SCALE INTEGRATION (VLSI) SYSTEMS, and IEEE TRANSACTIONS ON SIGNAL PROCESSING. He is also a member of the EURASIP SAT SPCN and IEEE CAS-VSATC.

Orion Afisiadis (Member, IEEE) received the Diploma degree in electrical and computer engineering from the Aristotle University of Thessaloniki, Thessaloniki, Greece, in 2015, and the Ph.D. degree in electrical engineering from the École Polytechnique Fédérale de Lausanne (EPFL), Lausanne, Switzerland, in 2020.

He is currently a Signal Processing Engineer with u-blox, Thalwil, Switzerland. His research interests include wireless communications for Internet of Things and 5G systems, in-band full-duplex wireless communications, signal processing for communications, and error-correction coding.